DNS Of entropy generation rates for turbulent flows subjected to high temperature gradients

J.M. Avellaneda, F. Bataille, A. Toutant, G. Flamant

▶ **To cite this version:**

J.M. Avellaneda, F. Bataille, A. Toutant, G. Flamant. DNS Of entropy generation rates for turbulent flows subjected to high temperature gradients. International Journal of Heat and Mass Transfer, 2021, 176, pp.121463. 10.1016/j.ijheatmasstransfer.2021.121463 . hal-03523271

HAL Id: hal-03523271

https://univ-perp.hal.science/hal-03523271

Submitted on 13 Jun 2023

HAL is a multi-disciplinary open access archive for the deposit and dissemination of scientific research documents, whether they are published or not. The documents may come from teaching and research institutions in France or abroad, or from public or private research centers.

L'archive ouverte pluridisciplinaire **HAL**, est destinée au dépôt et à la diffusion de documents scientifiques de niveau recherche, publiés ou non, émanant des établissements d'enseignement et de recherche français ou étrangers, des laboratoires publics ou privés.

Distributed under a Creative Commons Attribution - NonCommercial 4.0 International License

Version of Record: https://www.sciencedirect.com/science/article/pii/S0017931021005664
Manuscript_4f1b96ff371bdd5f1d1db10beda472fe

DNS of entropy generation rates for turbulent flows subjected to high temperature gradients

J.M. Avellaneda[a,*], F. Bataille[a], A. Toutant[a], G. Flamant[b]

[a] *PROMES-CNRS, UPR 8521, University of Perpignan Via Domitia, Perpignan, France*
[b] *PROMES-CNRS, UPR 8521, 7 rue du Four solaire, 66120 Font Romeu, France*

Abstract

Direct Numerical Simulations are performed to analyze the influence of key boundary conditions and flow characteristics on entropy generation rate statistics in a highly anisothermal forced convective turbulent channel flow of a thermo-dependent fluid submitted to asymmetrical heating. Each parameter is varied separately to quantify its influence compared to a reference simulation, the hot to cold wall temperature ratio from 1.5 to 3, the mean friction Reynolds number from 150 to 210, the mean thermodynamic pressure from 1 *bar* to 3 *bar*. Two thermal boundary condition types are also compared (fixed temperatures vs. fixed heat flux density at the walls). For each parameter that is varied, the evolution of the entropy generation rate mean, root-mean-square and correlations with the temperature and the streamwise or wall-normal velocity components are presented and discussed. All simulations have in common the thermal asymmetry and the highly non-isothermal nature of the flow: beyond the changes induced by the variation of each parameter, the common characteristics of the statistical quantity profiles are also analyzed. This work establishes how the spatial distribution of the local entropy generation rate is modified by the parameters studied, in which direction and with which sensitivity. It demonstrates the significant influence of the thermal boundary condition type on the entropy generation rate fluctuations near the walls.

Keywords: Direct Numerical Simulation, Entropy generation rate, Variable fluid properties, Asymmetrical heating

1. Introduction

Convective heat transfer is present in a large number of situations including natural systems, such as blood circulation with applications in medicine [1] or thermoregulation and thermal comfort of the human body [2]. Earth sciences are also concerned, such as geology [3] or volcanology [4]. It is also found in many man-made systems, where convective heat transfer flows can be internal ~~[5, 6] or external [7, 8] , laminar [9, 10] , transitional [11, 12] or turbulent [13, 14]~~ [5] or external [7] , laminar [9] , transitional [11] or turbulent [13] and correspond to natural ~~[15, 16] , forced [17, 18] or mixed [19, 20]~~ [15] , forced [17] or mixed [20] convection regimes. Restricting the scope to heat transfer in forced turbulent convective flows (which are the subject of this paper), engineering applications are implemented in automotive cooling systems [21], aeronautics and astronautics ~~[22, 23]~~ [22] , nuclear industry ~~[24, 25]~~ [25] or solar power plants ~~[26, 27]~~ [26] , to name just a few cases. These flows are complex due to the anisothermal and turbulent conditions: their study is carried out experimentally ~~[28, 29, 30, 17]~~ [30, 17] and also by using numerical simulations ~~[31, 32]~~ [31] , like RANS (Reynolds Averaged Numerical Simulations) ~~[33, 34]~~ [33] , LES (Large Eddy Simulations) ~~[35, 36, 37]~~ [37] or DNS (Direct Numerical Simulations) ~~[38, 39]~~ [39] that can be less expensive and helpful as a preparation approach before designing experiments. Direct Numerical Simulations [40], from the reference works carried in the 80′s [41], have demonstrated their usefulness in the detailed study of turbulent channel flows and as references [42, 43], either in the case of incompressible ~~[44, 45] or compressible [46, 47]~~ [44] or compressible [46] flows. In channel turbulent flows, many studies assume that the fluid properties are temperature-independent [48] and use symmetrical thermal boundary conditions ~~[49, 50, 51]~~ [49, 50] . However, there are situations in which the temperature gradients are high and the heating is asymmet-

*Corresponding author
Email address: jean-marc.avellaneda@promes.cnrs.fr (J.M. Avellaneda)

© 2021 published by Elsevier. This manuscript is made available under the CC BY NC user license
https://creativecommons.org/licenses/by-nc/4.0/

rical, as in the receivers of concentrated solar power plants [52, 53, 54, 55] [53, 54, 55] . In these situations, the temperature becomes an active scalar and the coupling between the differential equations governing the flow is more complex as temperature affects the momentum equation via the variation of the viscosity and the thermal conductivity in addition to the thermal dependence of the fluid density. This rich coupling between turbulent dynamic and thermal phenomena [56, 57, 58, 59] [56, 57, 58] demonstrates the theoretical interest of this type of flows, in addition to their practical applications in engineering. This is why, in the present paper, we consider the forced convective turbulent channel flow of a gas, which density, viscosity and thermal conductivity depend on temperature and that is subjected to high thermal gradients induced by asymmetrical heating boundary conditions.

In the context of this particular flow type, the emphasis is put on the local entropy generation rate field: DNS turbulent statistics (mean, root-mean-square and correlations) of the velocity and temperature fields have been the subject of previous research work [54, 60]. The local entropy generation rate is a key physical quantity revealing the level of local irreversibility in the different regions of the flow. Its integration determines the total entropy generation rate in the flow, which is an important criterion in engineering design and heat exchange optimization methods. For example, trade-offs between heat transfer enhancement and pressure drop reduction can be found by searching for a minimum in entropy generation and more generally, Entropy Generation Minimization [61, 62] can be applied to a large number of optimization configurations [63, 64]. Entropy-based optimization approaches use various methods such as variational calculus [65, 66, 67], genetic algorithms [68, 69] [68] or neural networks [70]. Beyond the total entropy generation rate in a flow, it is worth knowing the regions exhibiting the highest entropy generation rates to identify enhancement targets [71]. Similarly, it is useful to know the relative composition of the entropy generation rate, by nature of the underlying irreversibility (of viscous or heat transfer origin) [72], by direction (streamwise and wall-normal transfers in particular) and by evaluating the part due to the mean fields and the one due to their fluctuations. All these pieces of information bring a deeper knowledge of the physics of the flow and offer opportunities to build optimization strategies and to assess their effectiveness by comparison with a reference case. The evolution of the mean total entropy generated in the whole control volume is well known, when the parietal temperature ratio or the mean friction Reynolds number are increased, for example. The same is not true for the quantitative behavior of the local turbulent entropy generation rate field statistics (in the successive turbulent sublayers as well as in the center of the channel, in absolute and relative values and in composition) whose evolutions are less known, in particular for complex flows such as the one studied in the present paper, where the thermal/dynamic coupling is key. To the best of our knowledge, DNS simulation and statistical analysis of this local field as a function of boundary conditions and key flow characteristics has not been previously performed for a quasi-compressible asymmetric turbulent flow of a fluid with thermo-dependent physical properties.

The distribution of the local entropy generation rate, in magnitude and composition, in the different regions of the flow, depends on the thermal boundary conditions and key flow characteristics, like the hot to cold wall temperature ratio or the Reynolds number. This is why the core topic of this paper is to study their influence on the entropy generation rate statistics (its mean, standard deviation and correlations with the longitudinal and wall-normal velocity components) as functions of the distance to the channel walls. A set of Direct Numerical Simulations are performed to achieve this objective: first, a reference simulation corresponds to a hot to cold wall temperature ratio $T_2/T_1 = 2$ with fixed temperatures at the walls and a mean friction Reynolds number $Re_{\tau m} = 180$. Then, several Direct Numerical Simulations are carried out to analyze the influence of each key parameter, with an emphasis on thermal conditions, the parietal temperature ratio, the thermal boundary condition type (fixed wall temperatures vs. fixed wall heat flux density) but also on other important flow characteristics like the mean friction Reynolds number or the mean thermodynamic pressure.

2. Numerical method

2.1. Governing equations

We consider the forced convective three-dimensional fully-developed turbulent flow of a Newtonian gas with thermo-dependent viscosity, thermal conductivity and density. The flow regime is forced convection and no buoyancy effect is considered as the Richardson number for the studied simulations is small when compared to unity. The simulations presented correspond to a small Mach number $Ma \approx 10^{-2} << 1$ and the low Mach approximation can be applied to filter acoustic waves while keeping density variations due to temperature gradients [73]. In the case of an ideal gas, the correspond-

ing set of governing equations writes:

$$\frac{\partial \rho}{\partial t} + \frac{\partial (\rho U_j)}{\partial x_j} = 0 \tag{1}$$

$$\begin{aligned} \frac{\partial (\rho U_i)}{\partial t} + \frac{\partial (\rho U_i U_j)}{\partial x_j} = -\frac{\partial P_{dyn}}{\partial x_i} \\ + \frac{\partial}{\partial x_j}\left[\mu\left(\frac{\partial U_i}{\partial x_j} + \frac{\partial U_j}{\partial x_i}\right)\right] - \frac{2}{3}\frac{\partial}{\partial x_j}\left(\mu \frac{\partial U_k}{\partial x_k}\right) \end{aligned} \tag{2}$$

$$\rho C_p \left(\frac{\partial T}{\partial t} + U_j \frac{\partial T}{\partial x_j}\right) = \frac{\partial P_{th}}{\partial t} + \frac{\partial}{\partial x_j}\left(k \frac{\partial T}{\partial x_j}\right) \tag{3}$$

$$\frac{\partial P_{th}}{\partial x_i} = 0 \tag{4}$$

In Eqs. 1 to 4, the subscripts i and j obey Einstein's summation convention, x_i are the Cartesian coordinates, U_i are the components of the fluid velocity and t is the time. Thereafter x_1, x_2, x_3, U_1, U_2 and U_3 will be denoted x, y, z, U, V and W respectively. ρ is the density of the fluid, μ its dynamic viscosity, $C_p = 1005\ J.kg^{-1}.K^{-1}$ its heat capacity, k its thermal conductivity and T is its temperature. Pressure is the sum of two terms: $P = P_{dyn} + P_{th}$ where P_{dyn} (also named "dynamic pressure" hereafter) accounts for the variations of pressure due to the velocity and P_{th} (named "thermodynamic pressure" hereunder) is a uniform pressure linked to density and temperature via the equation of state of the fluid:

$$P_{th} = \rho r T \tag{5}$$

where $r = 287\ J.kg^{-1}K^{-1}$ is the specific gas constant. The dynamic viscosity depends on the temperature and obeys the Sutherland law that is valid in the working temperature range of the study [74]:

$$\mu = 1.461 \times 10^{-6} \frac{T^{1.5}}{T + 111} \tag{6}$$

The thermal conductivity also depends on the temperature and is derived from the dynamic viscosity and from the constant Prandtl number $Pr = 0.76$:

$$k = \frac{\mu C_p}{Pr} \tag{7}$$

The local entropy generation rate (by unit of volume, which is symbolized by a three-prime superscript) in the case of a homogeneous, non-reactive and electrically non-conductive fluid can be calculated using the following expression, where Φ is the viscous dissipation function [61]:

$$\dot{S}'''_{gen} = \frac{k}{T^2}(\nabla T)^2 + \frac{\Phi}{T} \tag{8}$$

$$\begin{aligned} \Phi = \mu\Big\{2\Big[(\frac{\partial U}{\partial x})^2 + (\frac{\partial V}{\partial y})^2 + (\frac{\partial W}{\partial z})^2\Big] \\ + (\frac{\partial U}{\partial y} + \frac{\partial V}{\partial x})^2 + (\frac{\partial U}{\partial z} + \frac{\partial W}{\partial x})^2 + (\frac{\partial V}{\partial z} + \frac{\partial W}{\partial y})^2 \\ - \frac{2}{3}(\frac{\partial U}{\partial x} + \frac{\partial V}{\partial y} + \frac{\partial W}{\partial z})^2\Big\} \end{aligned} \tag{9}$$

The total entropy generation rate (in $W.K^{-1}$) corresponds to the integration of $\dot{S}'''_{gen}$ over the whole fluid domain Ω:

$$\dot{S}_{gen} = \iiint_{\Omega} \dot{S}'''_{gen}.d\Omega \tag{10}$$

The entropy generation rate is the sum of the viscous friction ($\dot{S}'''_{gen,f}$) and the heat conduction ($\dot{S}'''_{gen,c}$) contributions,

$$\begin{aligned} \dot{S}'''_{gen} &= \dot{S}'''_{gen,c} + \dot{S}'''_{gen,f} \\ \dot{S}'''_{gen,c} &= \frac{k}{T^2}\Big[(\frac{\partial T}{\partial x})^2 + (\frac{\partial T}{\partial y})^2 + (\frac{\partial T}{\partial z})^2\Big] \\ \dot{S}'''_{gen,f} &= \frac{\Phi}{T} \end{aligned} \tag{11}$$

These two main parts can be broken-down into more elementary components. For example, the entropy generation rate due to heat conduction can be decomposed into the three directions of the thermal gradient:

$$\dot{S}'''_{gen,c} = \dot{S}'''_{gen,c,T_x} + \dot{S}'''_{gen,c,T_y} + \dot{S}'''_{gen,c,T_z} \tag{12}$$

$$\begin{aligned} \dot{S}'''_{gen,c,T_x} &= \frac{k}{T^2}(\frac{\partial T}{\partial x})^2 \\ \dot{S}'''_{gen,c,T_y} &= \frac{k}{T^2}(\frac{\partial T}{\partial y})^2 \\ \dot{S}'''_{gen,c,T_z} &= \frac{k}{T^2}(\frac{\partial T}{\partial z})^2 \end{aligned} \tag{13}$$

Similarly, the rate of entropy generation due to viscous friction is the sum of many terms (corresponding to the squares and cross products of components of the velocity gradient tensor). Asymmetrically heated channel flows exhibit preferred directions: the direction of flow, but also the direction normal to the walls for the wall-normal velocity component and for the derivatives of the temperature or the velocity components. A decomposition such as the one indicated in the Equation 13 allows a more refined analysis of the entropy generation rate. In Section 3, the main components of the entropy

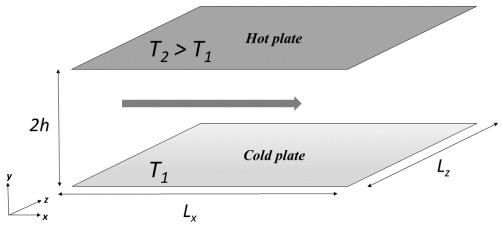

Figure 1: Bi-periodic flat plate channel

generation rate are identified and further decomposed into their part coming from the mean fields (temperature or velocity), on the one hand, and their part due to the turbulent fluctuations of these fields, on the other hand. The type of decomposition indicated in Equations 11 to 13 also applies to the analysis of the total entropy generation rate $\dot{S}_{gen}$, which includes a part related to viscous friction $\dot{S}_{gen,f}$ and another to heat transfer $\dot{S}_{gen,c}$ that can then be broken down further.

2.2. Numerical model

The fluid flows between two parallel flat plates. The longitudinal (Lx) and transversal (Lz) dimensions are periodic (Fig. 1). Bi-periodic plane channels in the longitudinal and transverse directions are commonly used in the study of turbulent shear flows because they allow to reach with a minimal computational cost a fully developed and statistically established flow in order to study the physical phenomena along the axis normal to the walls [75, 48] . A longitudinal body force, uniform in the channel and dynamically adjusted at each time step, is applied to compensate for frictional forces and maintain a constant mean mass flow rate [76] . The domain dimensions are $2\pi h \times 2h \times (\frac{4}{3})\pi h$ where $h = 0.014923\ m$. The mesh is made of $192 \times 190 \times 128$ cells. Meshing is uniform in the longitudinal and transversal directions. In the wall-normal direction, mesh size follows a hyperbolic tangential law to be finer close to the walls (Eq. 14), where N is the number of nodes over the the half-height of the channel (h) and a is a mesh dilatation parameter.

$$y_k = h\left\{1 + \frac{1}{a}\tanh\left[\left(-1 + \frac{k-1}{N-1}\right)\mathrm{artanh}(a)\right]\right\},\ k \in [1, N] \tag{14}$$

The reference Direct Numerical Simulation is performed at mean friction Reynolds number $Re_{\tau m} = 180$, where $Re_{\tau m}$ is the average of the friction Reynolds numbers at the walls (Eq. 15 and 16), which are in turn calculated from the corresponding friction velocities (Eq. 17). These are based on the spatio-temporal mean values at the walls (denoted by the $(\_)_w$ subscript) of the dynamic viscosity, density and the wall-normal gradient component of the mean longitudinal velocity. The reference DNS hot to cold wall temperature ratio is $T_2/T_1 = 2$ with $T_1 = 293\ K$ and wall temperatures are set uniform and constant at the walls. These thermal boundary conditions at the walls correspond to situations occurring, for example, in the surface receivers of concentrated solar power plants, where one side of a channel is exposed to a strong heating by solar radiation while the opposite side is insulated, resulting in the presence of a thermal gradient and a significant variation of the thermo-physical properties of the heat transfer fluid [58, 54] .

$$Re_{\tau m} = (Re_{\tau,cold} + Re_{\tau,hot})/2, \tag{15}$$

$$Re_{\tau,w} = \frac{U_{\tau,w} h}{\nu_w}, \tag{16}$$

$$U_{\tau,w} = \sqrt{\frac{<\mu_w>}{<\rho_w>}\left.\frac{\partial <U>}{\partial y}\right|_w} \tag{17}$$

Mesh sizes in wall units for the reference DNS are $\Delta x^+ = 4.6$ in the longitudinal direction, $\Delta z^+ = 4.6$ in the transversal direction and $\Delta y^+_{cold} = 0.47$, $\Delta y^+_{hot} = 0.20$ and $\Delta y^+_{center} = 2.9$ in wall-normal direction at the cold and hot wall and at the center of the channel respectively. As the boundary conditions are asymmetric, these dimensionless mesh sizes are the result of a normalization of real sizes by ν/U_τ, where ν and U_τ are the kinematic viscosity and the friction velocity at the corresponding walls for Δy^+_{cold} and Δy^+_{hot}, while the average kinematic viscosity and friction velocity between the cold and hot walls are used to normalize Δy^+_{center}, Δx^+ and Δz^+. The averaging time of the usual dynamic (e.g., velocity components, density, viscosity), thermal (e.g, temperature, thermal conductivity) and compound (e.g., correlations of the temperature and the velocity components) statistics (normalized by $h/U_{\tau m}$, where $U_{\tau m}$ is the mean friction velocity $U_{\tau m} = (U_{\tau,hot} + U_{\tau,cold})/2$), is $\Delta t^+ \approx 430$. The additional statistics, related to the local entropy generation rate mean, root-mean-square and correlations have been subjected

to a dimensionless integration time of $\Delta t^+_{EGR} \approx 110$. A mesh and domain size independence check has been performed with a finer mesh ($384 \times 266 \times 384$ with a $4\pi h \times 2h \times 2\pi h$ domain size) for the same mean friction Reynolds number $Re_{\tau m} = 180$, parietal temperature ratio $T_2/T_1 = 2$ and thermal boundary condition type (temperature are imposed at the walls). The finer mesh dimensionless sizes are: $\Delta x^+ = 4.6$, $\Delta z^+ = 2.3$, $\Delta y^+_{cold} = 0.25$, $\Delta y^+_{hot} = 0.10$ and $\Delta y^+_{center} = 2.3$. The reference simulation and the finer mesh one are in good agreement when comparing the velocity and temperature fields [60]. Similarly, friction velocities, temperatures (Eq. 18) and Reynolds numbers differ no more than 1.3 % between the reference simulation and the finer mesh one. The mesh and domain size independence is also valid for the entropy generation rate mean and root-mean-square as presented in Figs. 2(a) and 2(c) respectively. The dynamic and thermal fields of the presented simulations are in agreement with those of simulations performed on several meshes of gradual fineness [54] and the mesh sizes (in particular the first resolved point after the wall) are well positioned compared to literature simulations that have shown a good level of convergence at $Re_{\tau m} = 180$ [75] .

$$T_{\tau,w} = \frac{< k_w > \left.\frac{\partial <T>}{\partial y}\right|_w}{< \rho_w > C_p U_{\tau,w}} \tag{18}$$

To study the influence of the different thermal boundary conditions and flow characteristics in comparison with the reference simulation, a set of Direct Numerical Simulations is carried out by separately varying the temperature ratio, the mean friction Reynolds number, the type of thermal boundary conditions and the mean thermodynamic pressure. For example, a simulation with imposed wall heat flux is carried out with $Re_{\tau m} = 180$ and $T_2/T_1 = 2$ by setting a constant and uniform heat flux density at the walls corresponding to the mean one reached by the reference simulation ($\left|q''_w\right| \approx 1700\ W/m^2$). This fixed heat flux density simulation results in wall friction velocities and temperatures that do not differ from those of the reference simulation by more than 0.5 % and 1.2 % respectively, making them effectively comparable simulations. A finer mesh fixed heat flux density simulation has also been carried-out to check mesh and domain size independence for this thermal boundary condition type (see Figs. 2(b) and 2(d)). All simulations presented in Section 3 share the same domain size and mesh cell numbers than the reference simulation ($2\pi h \times 2h \times (\frac{4}{3})\pi h$ and $192 \times 190 \times 128$ respectively). The friction velocities, temperatures and Reynolds numbers at the hot or cold walls depend on the boundary conditions and flow characteristics: they are provided for each simulation in Appendix A (Table A.1). The corresponding dimensionless mesh sizes and integration times are listed in Appendix B (Table B.1).

All Direct Numerical Simulations are performed with the TrioCFD thermo-hydraulic code [77] created at the French Atomic and Alternative Energies Agency (CEA) and are carried-out on a High Performance Computing server provided by the French National Computing Center for Higher Education (CINES). Temperature diffusion and velocity diffusion and convection are handled by a second order centered scheme. A third order upstream QUICK scheme (Quadratic Upstream Interpolation for Convective Kinetics) is used for temperature convection. Time integration is performed via a third-order Runge-Kutta numerical scheme.

The different components of the numerical model have been verified with previous works. The same physical and numerical model has been used in a published work analyzing the influence of the thermal boundary condition on the statistics of the velocity and temperature mean, root-mean-square and correlations [60] . The thermo-hydraulic software has been used in many research works where numerical simulations are performed to study turbulent fluid flow coupled with other physical phenomena, including thermal transfer [58, 78, 54, 79] and the numerical schemes have been used in various works dealing with turbulent flow in a bi-periodic channel with active temperature scalar and asymmetric heating [58, 54] .

3. Results and discussion

In the following sections, the influence of the key boundary conditions and flow characteristics on the entropy generation rate statistics is described: the wall-temperature ratio in Section 3.1, the mean friction Reynolds number in Section 3.2, the thermal boundary condition type at the walls (fixed temperature vs. fixed heat flux density) in Section 3.3 and finally the mean thermodynamic pressure in Section 3.4. When studying the influence of one of these parameters, the others are kept constant at a reference value: $T_2/T_1 = 2.0$, $Re_{\tau m} = 180$, "Fixed temperatures at the walls" and $\langle P_{th} \rangle = 1.5\ bar$, in order to avoid cross effects. In each section, the following quantities are discussed successively: firstly, the mean $\left\langle \dot{S}'''_{gen} \right\rangle$ of the entropy generation rate (Eq. 19) and its standard-deviation (or root-mean-square) $[\dot{S}'''_{gen}]_{rms}$ (Eq. 20) are presented as a function of the distance to the cold wall. Indeed, since the

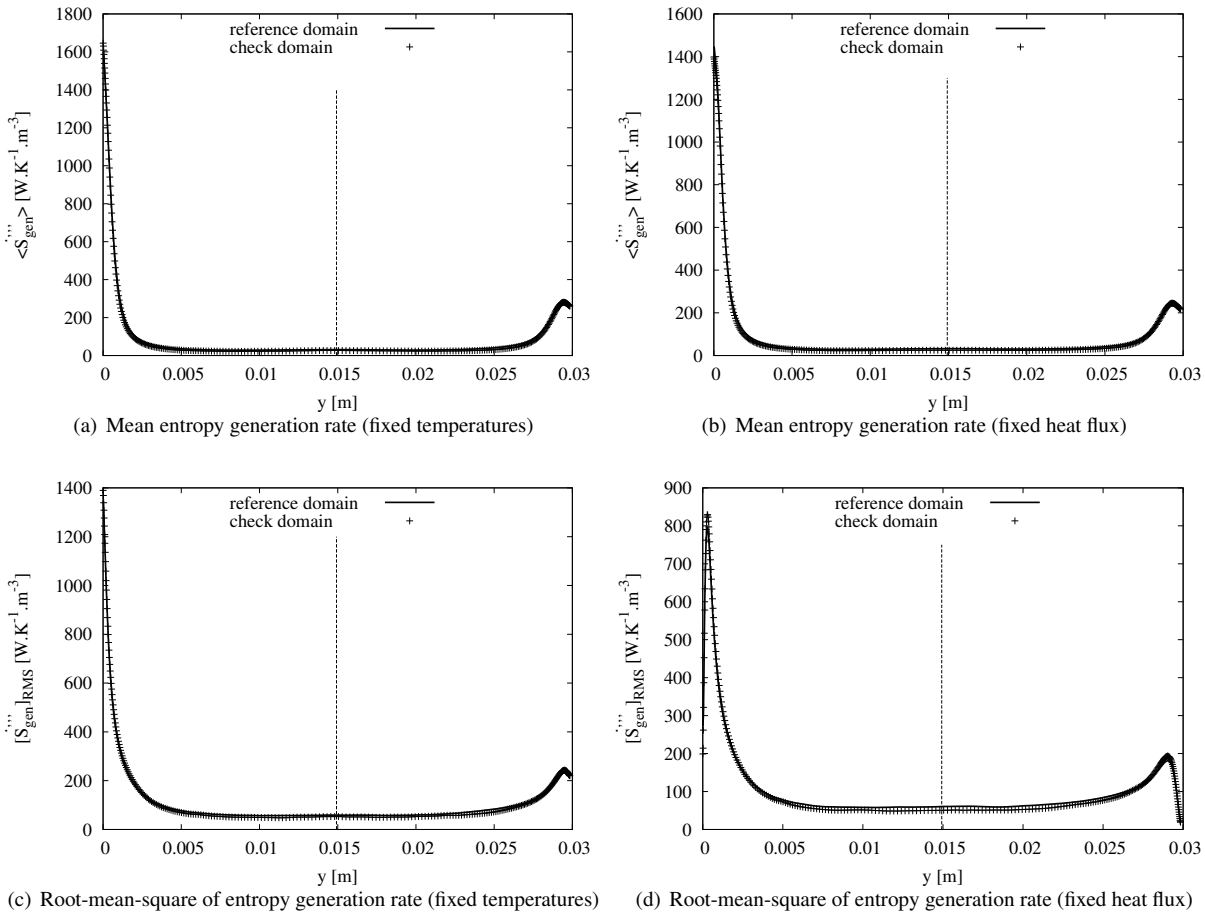

(a) Mean entropy generation rate (fixed temperatures)

(b) Mean entropy generation rate (fixed heat flux)

(c) Root-mean-square of entropy generation rate (fixed temperatures)

(d) Root-mean-square of entropy generation rate (fixed heat flux)

Figure 2: Grid and domain volume independence check: mean (on top line) and root-mean-square (on bottom line) of the entropy generation rate for two mesh definitions and domain sizes. Left: fixed wall temperatures. Right: fixed wall heat flux. The vertical dotted line indicates the position of the center of the channel. The cold and hot walls are located at $y = 0\ m$ and $y \approx 0.03\ m$ respectively.

channel is periodic in the longitudinal (resp. transverse) direction, the average values calculated on the planes perpendicular to this direction are independent of the x-coordinate (resp. z-coordinate) and the key analysis axis to study the statistical spatial distribution of the entropy generation rate is the axis normal to the walls (y-axis), which leads to the presentation of all statistics as functions of this spatial direction. Statistical averaging (written with brackets $< \_ >$) is done spatially over horizontal planes (i.e., xz planes, parallel to the walls) and over time. The mean entropy generation rate due to the vertical transfer of heat is then decomposed into the part due to the mean thermal field, on the one hand, and the part due to turbulent fluctuations, on the other hand (see Eqs. 22). These two components are presented in dimensionless form (Eq. 23) and as functions of the dimensionless distance to the closest wall (y^+, in Eq. 27).

Then, the same type of decomposition is used for the mean entropy generation rate by viscous friction due to the vertical gradient of the streamwise velocity component (see Eqs. 25 and 26). Finally, the correlation coefficients (see Eqs. 21) of the entropy generation rate with the temperature and the longitudinal or wall-normal velocity components are presented. The first section hereunder (3.1) is more developed, in addition to the impact analysis of the wall temperature ratio, the common shape of the curves ($\left\langle \dot{S}'''_{gen} \right\rangle$, $[\dot{S}'''_{gen}]_{rms}$ etc.) is described and analyzed. The following sections then focus almost exclusively on the study of the influence of the corresponding flow characteristics. The analyzed quantities are defined as follows,

$$\left\langle \dot{S}'''_{gen}(x,y,z,t) \right\rangle = \left\langle \left\langle \dot{S}'''_{gen}(x,y,z,t) \right\rangle_{xz} \right\rangle_{t} \qquad (19)$$

$$[\dot{S}'''_{gen}]_{rms} = \sqrt{< (\dot{S}'''_{gen})^2 > - < \dot{S}'''_{gen} >^2} \quad (20)$$

$$\begin{aligned} R_{\dot{S}'''_{gen},T} &= \frac{\left\langle \dot{S}'''_{gen} T \right\rangle - \left\langle \dot{S}'''_{gen} \right\rangle \langle T \rangle}{[\dot{S}'''_{gen}]_{rms} T_{rms}} \\ R_{\dot{S}'''_{gen},U} &= \frac{\left\langle \dot{S}'''_{gen} U \right\rangle - \left\langle \dot{S}'''_{gen} \right\rangle \langle U \rangle}{[\dot{S}'''_{gen}]_{rms} U_{rms}} \\ R_{\dot{S}'''_{gen},V} &= \frac{\left\langle \dot{S}'''_{gen} V \right\rangle - \left\langle \dot{S}'''_{gen} \right\rangle \langle V \rangle}{[\dot{S}'''_{gen}]_{rms} V_{rms}} \end{aligned} \quad (21)$$

$$\begin{aligned} \left\langle \dot{S}'''_{gen,c,T_y} \right\rangle &= \dot{S}'''_{gen,c,T_y,MEAN} + \dot{S}'''_{gen,c,T_y,FLUCT} \\ \dot{S}'''_{gen,c,T_y,MEAN} &= \frac{< k >}{< T >^2} \left(\frac{d < T >}{dy} \right)^2 \\ \dot{S}'''_{gen,c,T_y,FLUCT} &= < \dot{S}'''_{gen,c,T_y} > - \dot{S}'''_{gen,c,T_y,MEAN} \end{aligned} \quad (22)$$

$$< \dot{S}'''_{gen,c} >^+ = \frac{< \dot{S}'''_{gen,c} >}{< q''_w >^2 / (k_w < T_w >^2)} \quad (23)$$

$$\dot{S}'''_{gen,f,u_y} = \frac{\mu}{T} \left(\frac{\partial U}{\partial y} \right)^2 \quad (24)$$

$$\begin{aligned} \left\langle \dot{S}'''_{gen,f,u_y} \right\rangle &= \dot{S}'''_{gen,f,u_y,MEAN} + \dot{S}'''_{gen,f,u_y,FLUCT} \\ \dot{S}'''_{gen,f,u_y,MEAN} &= \frac{< \mu >}{< T >} \left(\frac{d < U >}{dy} \right)^2 \\ \dot{S}'''_{gen,f,u_y,FLUCT} &= < \dot{S}'''_{gen,f,u_y} > - \dot{S}'''_{gen,f,u_y,MEAN} \end{aligned} \quad (25)$$

$$< \dot{S}'''_{gen,f} >^+ = \frac{< \dot{S}'''_{gen,f} >}{< \mu_w > U^4_{\tau,w} / (< \nu_w >^2 < T_w >)} \quad (26)$$

$$y^+ = \frac{y_w U_{\tau,w}}{\nu_w} \quad (27)$$

3.1. Influence of the wall temperature ratio

Four simulations are performed to analyze the influence of the hot to cold wall temperature ratio on the entropy generation rate field, while keeping the mean friction Reynolds number at 180. For all simulations, the temperature of the cold wall $T_1 = 293\ K$ is uniform and constant. The four Direct Numerical Simulations correspond to four different uniform and constant hot wall temperatures: $T_2/T_1 = 1.5$ with $T_2 = 439.5\ K$, $T_2/T_1 = 2.0$ with $T_2 = 586\ K$, $T_2/T_1 = 2.5$ with $T_2 = 732.5\ K$ and finally $T_2/T_1 = 3.0$ with $T_2 = 879\ K$. The temperature gap between the hot and cold walls thus varies from 146.5 K to 586 K, which allows to observe significant changes on the entropy generation rate and on the thermo-physical properties of the fluid. When the temperature changes from 293 K to 879 K, the density of the fluid is divided by 3, the dynamic viscosity and the thermal conductivity are multiplied by ≈ 2 and the kinematic viscosity is ≈ 6 times greater. The thermal conductivity relative variation is significantly less ($\approx +10\%$) and it is the same for the molecular Prandtl number ($\approx -2\%$) or the heat capacity ratio $\gamma = C_p/C_v$ ($\approx -4\%$) that are all three considered constant. As the hot to cold wall temperature ratio increases, the computer resource and computation time increase altogether as the stability time step, required for simulation convergence, is reduced: in this paper, the maximum temperature ratio is $T_2/T_1 = 3$, so that the behavior of the entropy generation statistics can be observed while keeping high performance computing consumption within reasonable limits. As the core of the present work is to examine situations where gradients are significant, wall temperature ratios under 1.5 are not presented. As T_2/T_1 approaches 1 (the isothermal case), the entropy generation rate reaches a symmetrical profile dominated by the entropy generation due to viscous friction.

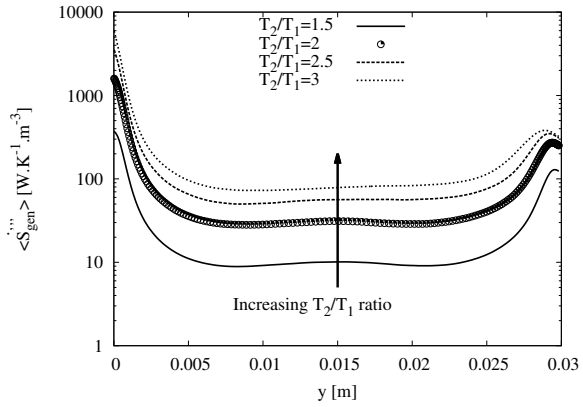

Figure 3: Mean local entropy generation rate as a function of the distance to the bottom (cold) wall for different wall temperature ratios.

When the hot to cold wall temperature ratio increases, the mean local entropy generation rate is larger whatever the distance from the cold wall (Fig. 3), at the walls but also at the center of the channel. The entropy generation rates are higher near the walls and particularly near the cold one. These are indeed the regions where temperature and velocity gradients are the highest. The profiles are asymmetric: the mean entropy generation rate is higher at the cold wall than at the hot one es-

sentially because the temperature (and the thermal conductivity) is lower while the mean heat flux densities at the cold and hot walls are identical when steady-state is achieved on average. Indeed, the average entropy generation rate at the walls depends primarily on the contribution due to the vertical temperature gradient $\left\langle (kT^2)(\partial T/\partial y)^2 \right\rangle$, which can be expressed as a function of the heat flux q_x crossing the wall: $\left\langle q_x^2/(kT^2) \right\rangle$. Thus, a lower temperature at the wall (for the same average heat flux) corresponds to an increase in the average entropy generation rate via a direct effect of the $1/T^2$ factor and an indirect effect of the $1/k$ one since the thermal conductivity increases with temperature.

Table 1: Influence of the wall-temperature ratio T_2/T_1 on the asymmetry of the mean local entropy generation rate profile (Fig. 3). The following ratios of $< \dot{S}'''_{gen} >$ are reported: between the cold and the hot wall (**Cold/Hot**), between the cold wall and the center of the channel where $y = h$ (**Cold/Center**) and finally between the hot wall and the center of the channel (**Hot/Center**).

T_2/T_1	**Cold/Hot**	**Cold/Center**	**Hot/Center**
1.5	3.0	36.8	12.2
2.0	6.4	51.3	8.1
2.5	11.4	62.6	5.5
3.0	18.3	75.6	4.1

The cold to hot wall asymmetry increases with the wall-temperature ratio (see Table 1): the ratio of mean entropy generation rate between the cold wall and the hot wall increases from 3.0 to 18.3 when T_2/T_1 is varied from 1.5 to 3.0. The same asymmetry increase is observed for the ratio of mean entropy generation rate between the cold wall and the center of the channel ($y = h$) but to a lesser extent as it is multiplied by ≈ 2 (while the wall entropy generation rate ratio is multiplied by ≈ 6). Conversely, the ratio of mean entropy generation rate between the hot wall and the center of the channel decreases when T_2/T_1 gets larger (it is divided by ≈ 3) when the wall-temperature ratio jumps from 1.5 to 3.0. Indeed, the relative increase of the wall mean entropy generation rate is higher at the cold wall than at the hot one for the same increase of the wall-temperature ratio, particularly when the latter is high. If T_2/T_1 is raised from 2.5 to 3.0, the cold wall and hot wall mean entropy generation rates increase by approximatively 68% and 4.6% respectively (and the relative increase at the center of the channel is 39%).

A local maximum of the mean entropy generation rate exists near the hot wall (Fig. 3). Mean entropy generation rate local maximums close to the walls are also reported in research works based upon DNS in flat plate turbulent channel flows [80, 72]. Close to the cold wall, the temperature increases while its vertical gradient decreases when moving away from the wall and both variations result in a decrease of the mean entropy generation rate. Conversely, very close to the hot wall the conductive heat flux varies little while the temperature decreases, which leads to an increase of the entropy generation rate. Moving further away from the hot wall, the decreasing slope of k/T^2 and $(\partial T/\partial y)^2$ means become equal and the local maximum of $< \dot{S}'''_{gen} >$ is reached, after which the square of the vertical temperature gradient decreases faster than k/T^2, resulting in a decreasing entropy generation rate as the distance to the hot wall keeps increasing. The position of the local maximum is closer to the wall for small values of the wall-temperature ratio (a behavior also observed for the local maximum of the entropy generation rate in the boundary-layer of an incompressible fluid above a heating flat plate [81]). When T_2/T_1 is increased from 1.5 to 3.0, the distance of the local maximum to the hot wall is increased form $\approx 1.8 \times 10^{-2}h$ to $\approx 6.4 \times 10^{-2}h$ (where h is the channel half-width), which corresponds to $y+ \approx 2.4$ and $y+ \approx 4.6$ in dimensionless wall units. The dimensionless position of the mean entropy generation rate local maximum is approximatively related to the wall-temperature ratio by the relation $y^+ \approx 1.45 \times (T_2/T_1) + 0.23$ with a good linear correlation ($R^2 = 0.998$) within the interval $[1.5; 3.0]$ of T_2/T_1. This empirical linear regression relation is no longer valid when the wall temperature ratio is close to 1, for instance when $T_2/T_1 = 1.01$, as the mean entropy generation rate is then essentially due to viscous friction. Moreover, if $T_2/T_1 \approx 1$ the mean entropy generation rate is no longer flat in the central region of the channel (as in Fig. 3) but exhibits a minimum around the center of the channel because the entropy generation rate due to viscous friction is related to the wall-normal gradient of the longitudinal velocity, which value vanishes when this velocity component reaches its maximum.

The standard deviation (or RMS : Root-Mean-Square) of the entropy generation rate as a function of the distance to the cold wall is presented in Fig. 4 for different wall-temperature ratios. The observations mentioned above for the mean entropy generation rate also apply to its root-mean-square: an increase of T_2/T_1 also results in an increase of the standard deviation of the entropy generation for any ordinate y, more hot to cold wall asymmetry and a move of the hot side local maximum further from the hot wall. The positions in wall units of the local maximums near the hot wall are close

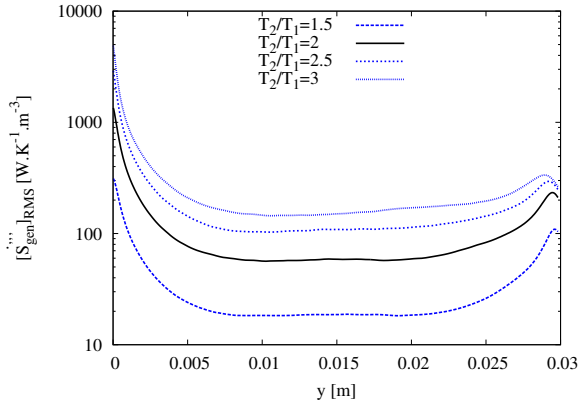

Figure 4: Root-mean-square of the entropy generation rate as a function of the distance to the bottom (cold) wall for different wall temperature ratios.

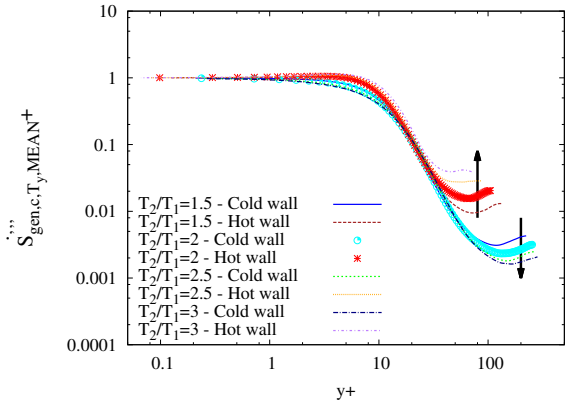

(a) Entropy generation from flow mean fields

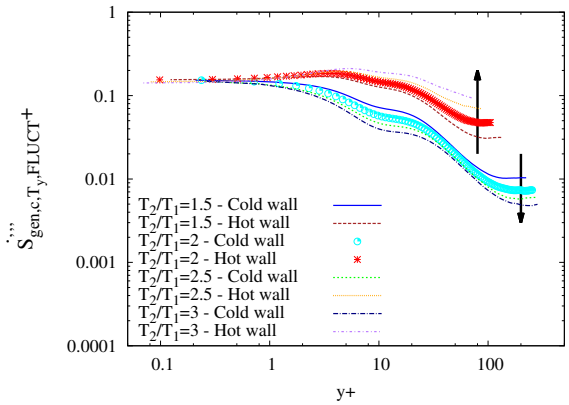

(b) Entropy generation from fluctuations

Figure 5: Decomposition of the dimensionless mean local entropy generation rate by vertical heat conduction (cf. Eqs. 22 and 23). The black arrows indicate the direction of change as T_2/T_1 increases.

to the ones observed for the entropy generation rate mean (the gap staying between 0% and −13% depending on the simulation, which may be non-significant because the RMS convergence is slower than the mean). All in all, the profiles and the order of magnitudes of the entropy generation rate RMS, on the one hand, and mean, on the other hand, are similar. Nevertheless, the RMS are lower than the mean near the walls (≈ −20%) and higher in the central region of the channel (≈ +90%).

The total entropy generation rate in the channel $\dot{S}_{gen}$ (Eq. 10) is largely dominated by the heat transfer irreversibility. In the present situations, where thermal gradients are high while Reynolds numbers are moderate, the total entropy generation rate due to viscous friction accounts for about 0.08 % and 0.01 % of the total entropy generation rate when the wall temperature ratio are $T_2/T_1 = 1.5$ and 3 respectively. Whatever the wall temperature ratio (between 1.5 and 3), about 80 % of the total entropy generation rate is due to the vertical heat conduction. Moreover, since the temperature is imposed at the walls, its gradient in the longitudinal and transverse directions is zero at the walls and the corresponding components of the entropy generation rate ($\dot{S}'''_{gen,c,T_x}$ and $\dot{S}'''_{gen,c,T_z}$ in Eqs. 13) are also zero at the walls. Thus, $\dot{S}'''_{gen,c,T_y}$ is the only significant contributor to the mean wall entropy generation rate. As indicated in Section 2.1, the mean entropy generation rate due to wall-normal heat transfer can be decomposed into two terms: the part due to the mean fields $\dot{S}'''_{gen,c,T_y,MEAN}$ (the mean temperature, which determines its mean vertical gradient, and the mean thermal conductivity), on the one hand, and the part due to turbulent fluctuations of these fields $\dot{S}'''_{gen,c,T_y,FLUCT}$ (see Eqs. 22), on the other hand. The profile of these two components are presented in Fig. 5(a) and 5(b) respectively, in dimensionless form (Eq.23) as functions of the dimensionless distance to the nearest wall y^+ (Eq. 27). The highest entropy generation rates are concentrated in the near wall region and more precisely in the viscous sublayer ($y+ \leq 5$). The dimensionless mean field contribution (Fig. 5(a)) stays close to its value at the walls and in the viscous sublayer, decreases rapidly in the buffer region and more slowly in the major part of the logarithmic sublayer. At the minimum, the dimensionless entropy generation rates by vertical heat conduction due to mean fields are about 3 and 2 orders of magnitude lower than at the corresponding walls on the cold and hot sides of the channel respectively. $\dot{S}'''_{gen,c,T_y,MEAN}$ is increasing in the rest of the logarithmic zone and in the outer region, which would not be the case for a symmetrically heated chan-

nel [80, 72]. The wall-temperature ratio affects mainly the logarithmic and outer regions (i.e., when $y+ \gtrapprox 30$ on the hot side and $y+ \gtrapprox 50$ on the cold side). An increase of T_2/T_1 results in an increase of $\dot{S}'''_{gen,c,T_y,MEAN}$ in both regions on the hot side of the channel and a decrease on the cold side. These observations are in agreement with the discussion about Table 1: as the wall-temperature ratio increases, the mean entropy generation rate ratio between the cold wall and the center of the channel is increasing, while the corresponding ratio on the hot side of the channel is decreasing.

At the walls, the relative part of the wall-normal heat transfer mean entropy generation rate due to fluctuations of the thermal field $\dot{S}'''_{gen,c,T_y,FLUCT}$ corresponds approximatively to 15% of the part due to the mean fields. (Fig. 5(b)). The hot to cold wall asymmetry increase induced by the wall temperature ratio starts as soon as $y+ \gtrapprox 0.5$, i.e., earlier than for $\dot{S}'''_{gen,c,T_y,MEAN}$. On the cold side, $\dot{S}'''_{gen,c,T_y,FLUCT}$ is a decreasing function of y^+, although the dropping rate exhibits variations: an oscillation occurs in the buffer sublayer and smooth slopes are present in the end of the logarithmic region and in the outer zone. Oscillations of the fluctuating part near the walls are also reported in other research works dealing with entropy generation in turbulent shear flows [80, 72]. In the hot side of the channel, $\dot{S}'''_{gen,c,T_y,FLUCT}$ starts increasing up to a maximum value located within the viscous sublayer. Then, still in the hot side, the mean vertical heat conduction entropy generation rate due to fluctuations decreases and exhibits a profile similar to the one in the cold side, but at higher relative values with respect to the magnitude at the wall. On both sides of the channel, the decay is mostly slower for $\dot{S}'''_{gen,c,T_y,FLUCT}$ than for $\dot{S}'''_{gen,c,T_y,MEAN}$ and the relative importance of the fluctuating part with respect to the mean part increases (for the same y^+ position). This is to be related to the observation made above about the standard deviation of the entropy generation rate that is higher than the mean in the central region of the channel.

Although entropy generation in the channel is largely dominated by heat transfer, it is worth observing the viscous component because dynamical and thermal phenomena are coupled and because a reference is required to assess potential flow channel modifications aiming to, for example, intensify heat transfer, but which may also increase viscous friction. An increase in the wall temperature ratio results in an increase of the mean local viscous friction entropy generation rate $\left\langle \dot{S}'''_{gen,f} \right\rangle$ except close to the hot wall where it becomes smaller. The total viscous entropy generation rate $\dot{S}_{gen,f}$ is essentially

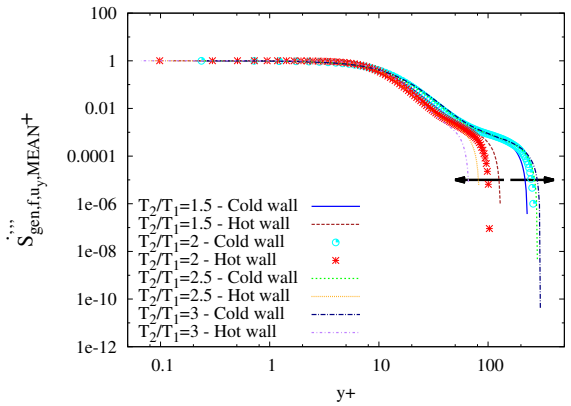

(a) Entropy generation from flow mean fields

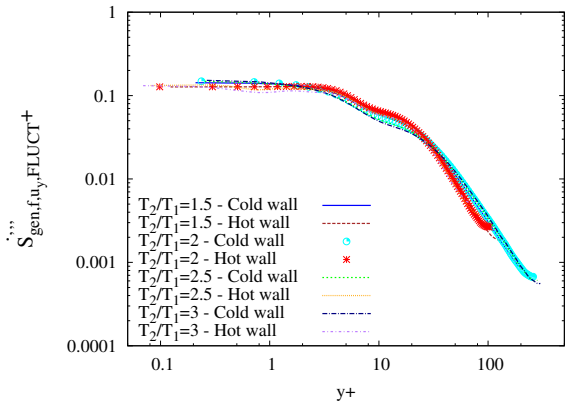

(b) Entropy generation from fluctuations

Figure 6: Decomposition of the dimensionless mean local entropy generation rate by viscous friction due to the wall-normal gradient of the streamwise velocity component (cf. Eqs. 25 and 26). The black arrows indicate the direction of change as T_2/T_1 increases.

due to the vertical gradient of the longitudinal velocity component $\dot{S}'''_{gen,f,u_y}$ in Eq. 24, which accounts for 80 % of $\dot{S}_{gen,f}$ once integrated over the channel volume and that is presented in Figs. 6. In dimensionless values, the profile of the part due to the turbulent fluctuations (6(b)) is little affected by the wall temperature ratio. For a given value of y^+, the order of magnitude of $\dot{S}'''_{gen,f,u_y,FLUCT}$ is the same whatever T_2/T_1, in the studied range [1.5; 3.0]. Conversely, the part due to the mean velocity and temperature fields $\dot{S}'''_{gen,f,u_y,MEAN_+}$ (6(a)) exhibits an asymmetry and a dispersion of the curves in the center of the channel. Indeed, as the wall temperature ratio gets greater, the cold wall friction Reynolds number increases (which pushes the maximum value of y+ to greater values), while the hot wall friction Reynolds number decreases and has the opposite effect (see Table A.1 in Appendix A). The same ordinate position y

at the center of the channel thus leads to more and more separated values of the corresponding y^+_{cold} and y^+_{hot} dimensionless distances to the walls, which increases the hot/cold side asymmetry in Fig. 6(a). In addition to the friction Reynolds number effect cited above, it must be noted that the vertical portions of the curves correspond to the real positions (ordinates y) where the mean longitudinal velocity is maximum and $d\langle U\rangle/dy$ vanishes. This vanishing position is located after the geometrical middle of the channel ($y = h$) and is pushed further this center in the direction of the hot wall as the wall temperature ratio increases. For this reason, in Figs 6, the hot and cold sides are defined relatively to this vanishing position.

The profiles of the correlation coefficients of the entropy generation rate with the temperature or the longitudinal or wall-normal velocity components, depend little on the wall-temperature ratio (Figs. 7). Nevertheless, a horizontal translation of the cold and hot side curves occurs towards greater and lower y^+ respectively when T_2/T_1 increases. This translation corresponds to the wall friction Reynolds number evolution that increases on the cold side with T_2/T_1, while it decreases on the hot side. When $y^+ \gtrapprox 20$, the correlation coefficients are closer to zero because the corresponding fluctuation correlations (or covariances) are near zero in this region far enough from the walls, while the root-mean-squares of the temperature or the velocity components are non-zero. For example, $\left|R_{\dot{S}'''_{gen},T}\right| < 0.12$ if $y^+ \gtrapprox 20$. Near the walls (in the viscous sublayer), the correlation coefficient of the entropy generation rate with the temperature (Fig. 7(a)) is approximatively 1 in absolute value. This coefficient is positive at the cold wall and negative at the hot one. Very close to the cold wall, a positive temperature fluctuation (i.e. an instantaneous local temperature above the mean: $T = \langle T\rangle + T'$ with $T' > 0$) induces an increase of the vertical gradient of the temperature, which results in an increase of the entropy generation rate ($(\partial T/\partial y)^2$ is the determinant factor, k/T^2 decreases and other terms of the entropy generation rate also vary but their influence is secondary). Conversely, very close to the hot wall, a positive temperature fluctuation reduces the thermal gap with the wall and results in a decrease of the entropy generation rate, hence the negative value of the correlation coefficient. The correlation coefficients of the entropy generation rate with the longitudinal and wall-normal velocity components near the walls are directly related to the correlations of the temperature with these two velocity components. Because $R_{\dot{S}'''_{gen},T} \approx 1$ near the cold wall, $R_{\dot{S}'''_{gen},U} \approx R_{T,U}$. For the same reason, as $R_{\dot{S}'''_{gen},T} \approx -1$ near the hot wall, $R_{\dot{S}'''_{gen},V} \approx -R_{T,V}$. Since the correlation coefficient between the temperature and the longitudinal velocity is positive on the cold side and negative on the hot side with almost the same absolute value (≈ 0.9), it follows

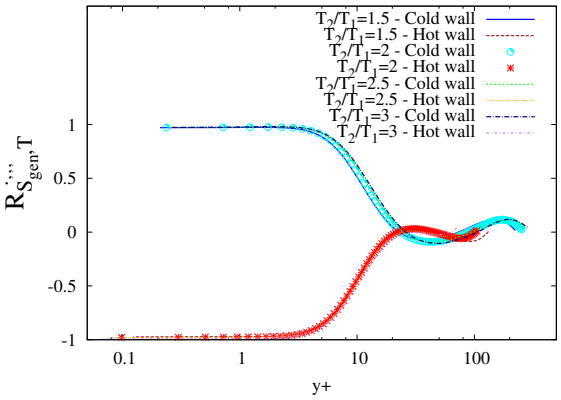

(a) Correlation with the temperature

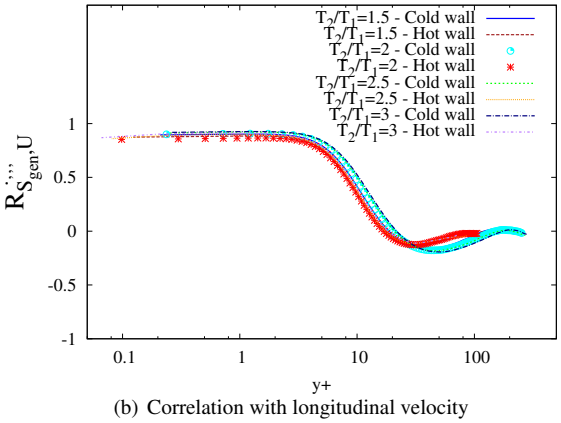

(b) Correlation with longitudinal velocity

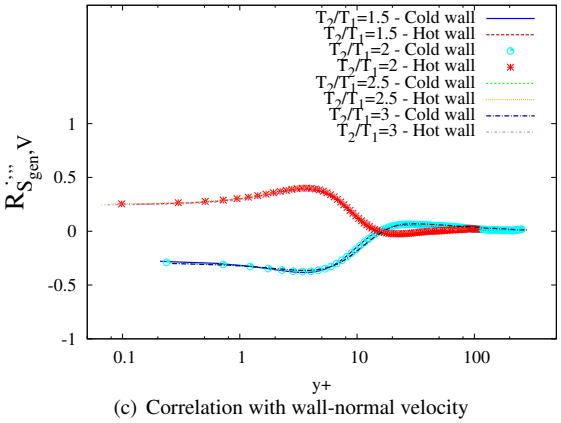

(c) Correlation with wall-normal velocity

Figure 7: Correlation coefficients of the local entropy generation rate with the temperature (a), the streamwise velocity component (b) and the wall-normal velocity component (c).

that $R_{\dot{S}'''_{gen},U}$ is positive near both walls and exhibits close values ($\approx$ 0.9 also). The same reasoning explains the sign and the order of magnitude of $R_{\dot{S}'''_{gen},V}$ near the walls: $R_{T,V}$ is always negative and around -0.23 at the walls. Consequently, the correlation coefficient of the entropy generation rate and the wall-normal velocity is negative on the cold side and positive on the hot side. Its absolute value is ≈ 0.27.

3.2. Influence of the mean friction Reynolds number

In this section, the mean friction Reynolds number is varied while keeping the wall temperature ratio to 2.0 and the cold wall temperature to 293 K. Three Direct Numerical Simulations are performed at $Re_{\tau m}$ = 150, 180 and 210. These values allow exhibiting changes in the entropy generation rate statistics, while staying in the region of low to moderate Reynolds number so that thermal effects keep being dominant.

Increasing the mean friction Reynolds number results in a rise of the mean entropy generation rate near and at the walls (Figs. 8). Varying $Re_{\tau m}$ from 150 to 210 induces an increase of $\left\langle \dot{S}'''_{gen} \right\rangle$ by $\approx$ 74 % at the cold and hot walls, which does not change the cold/hot wall asymmetry. This relative increase is in agreement with the one of $(U_\tau T_\tau)^2$ that rules the increase of the majority component in wall entropy generation rate (due to the wall-normal conduction of heat) and can be deduced from the laws at the wall. Since the friction temperature changes little for the Reynolds number range studied (see Table B.1 in Appendix A), the evolution of $\left\langle \dot{S}'''_{gen} \right\rangle$ at the walls is dominated by the relative increase in the square of the friction velocity at each wall ($\approx$ +93 % when $Re_{\tau m}$ raises from 150 to 210), slightly dampened by the corresponding relative decrease in the square of the friction temperature (≈ -10 %). In a large central region of the channel (80% of its height: from $y = h/10$ to $y = 19h/10$, in half-channel height units) the mean entropy generation rate is less changed by the variation of the mean friction Reynolds number, can be negative or positive (it stays between -14 % to +20 %) and concerns values that are relatively very small compared to the entropy generation rates near the walls. Thus, the variation of the mean friction Reynolds number mainly influences the near-wall regions, where the highest entropy generation rates are located. The position of the entropy generation rate local maximum on the hot side of the channel gets closer to the hot wall when the $Re_{\tau m}$ is increased: it is located at $\approx 0.04h$ and $\approx 0.026h$ of the hot wall (in channel half-height units) when the mean friction Reynolds numbers are 150 and 210 respectively. This position is more stable when expressed in wall units ($y^+ \approx 3.6$ at $Re_{\tau m} = 150$ and $y^+ \approx 3.2$ at $Re_{\tau m} = 210$) because the friction Reynolds number at the hot wall increases in the ratio 210/150 (see Table A.1). Similarly, it is relatively stable (slightly decreasing with $Re_{\tau m}$) when applying a local scaling $y^\star = y_w U_{\tau,hot}/\nu$, where ν is the mean kinematic viscosity when $\dot{S}'''_{gen}$ reaches its local maximum: $y^\star \approx 3.9$ at $Re_{\tau m} = 150$ and $y^\star \approx 3.4$ at $Re_{\tau m} = 210$

The root-mean-square of the entropy generation rate (Fig. 9) reacts qualitatively in the same way than its mean. It increases at the walls with the mean friction Reynolds number and changes relatively less in the central region of the channel. The local maximum on the hot side also comes closer to the wall (in half height or wall units) when the mean friction Reynolds number increases from 150 to 210.

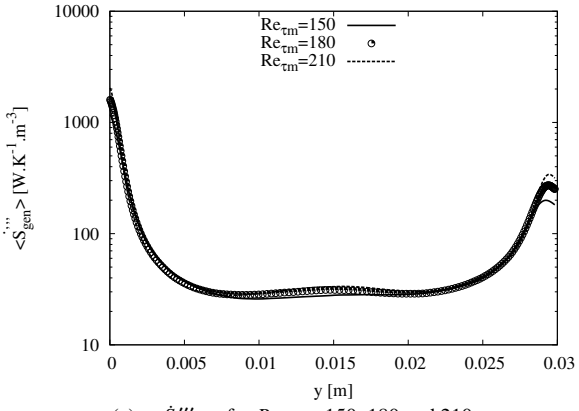

(a) $< \dot{S}'''_{gen} >$ for $Re_{\tau m}$ = 150, 180 and 210

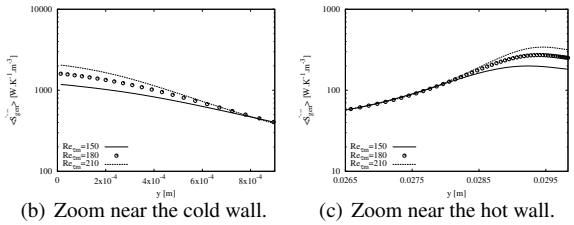

(b) Zoom near the cold wall. (c) Zoom near the hot wall.

Figure 8: Mean local entropy generation rate as a function of distance to the bottom (cold) wall for different mean friction Reynolds numbers $Re_{\tau m}$ (Eq. 15)

As observed in Section 3.1, the main component in the total entropy generation rate is due to the entropy generated by heat transfer (viscous terms are several orders of magnitude less) and more particularly by the wall-normal conduction of heat. Longitudinal and transversal gradients of the temperature have to be accounted for in the central region of the channel as they are of the same order of magnitude than vertical ones,

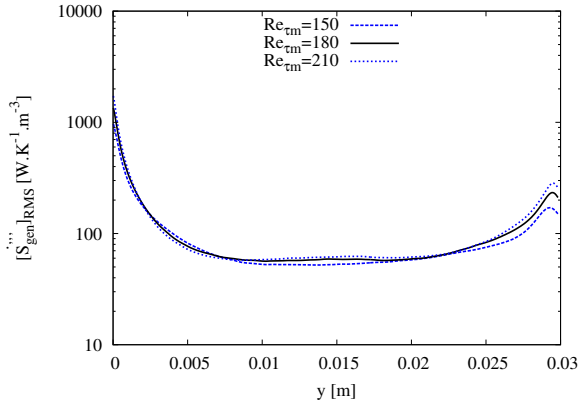

Figure 9: Root-mean-square of the entropy generation rate as a function of the distance to the bottom (cold) wall for different mean friction Reynolds numbers.

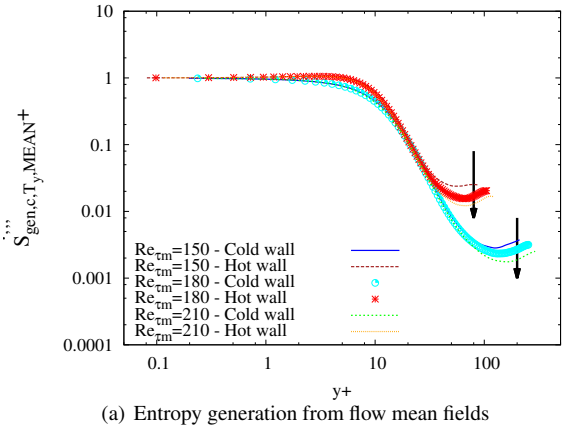

(a) Entropy generation from flow mean fields

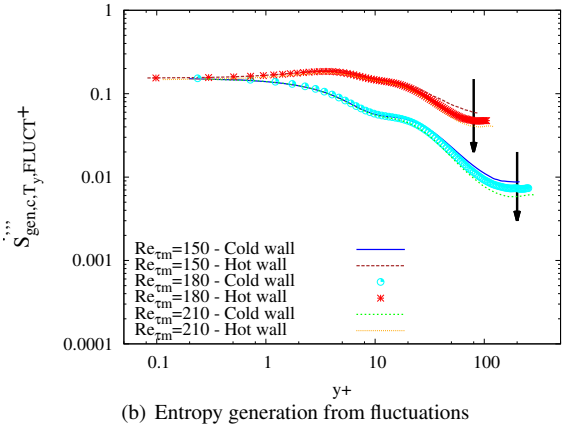

(b) Entropy generation from fluctuations

Figure 10: Decomposition of the dimensionless mean local entropy generation rate by vertical heat conduction (cf. Eqs. 22 and 23). The black arrows indicate the direction of change as $Re_{\tau m}$ increases.

but all contributions in this region are very low when compared to the entropy generation rates in the wall vicinities. All these remarks stay true when varying $Re_{\tau m}$ from 150 to 210, hence the interest in analyzing the behavior of the dominant term $\left\langle \dot{S}'''_{gen,c,T_y} \right\rangle$ (Eq. 13). This majority term (once made dimensionless: Eq. 23) is decomposed as explained before in the part due to the mean temperature field and the part due to its fluctuations (Eq. 22). The general shape of these two parts are similar to the one observed and described in Section 3.1. The effect of the mean friction Reynolds number variations starts to be significant (for the studied range) approximately from the beginning of the buffer sublayer, both for the mean (Fig. 10(a)) and the fluctuation (Fig. 10(b)) parts. Both parts then decrease as $Re_{\tau m}$ increases from 150 to 210. In the buffer, logarithmic and outer regions, the entropy generation rate due to vertical heat conduction decreases relative to its values at the walls. This observation is in agreement with the increasing cold/center and hot/center ratios of the mean entropy generation rate in Figure 8(a).

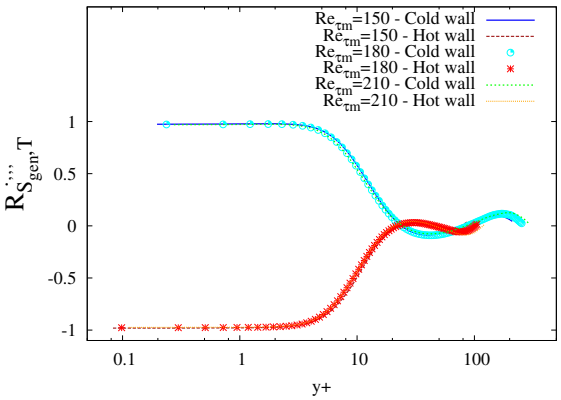

Figure 11: Correlation coefficient of the entropy generation rate with the temperature for $Re_{\tau m}$ = 150, 180 and 210.

The correlation coefficients of the entropy generation rate with the temperature, the longitudinal velocity or the wall-normal velocity are not significantly changed by an increase of the mean friction number from 150 to 210 (a +40% increase). As an illustration, the correlation with the temperature is presented in Fig. 11. This confirms the stability of these correlation coefficient profiles, as was observed in Section 3.1. Similarly, at the walls, the correlation coefficients of the entropy generation rate with the longitudinal and wall-normal velocity components exhibit absolute values close to those of $R_{T,U}$ and $R_{T,V}$ respectively. The positive or negative sign of $R_{\dot{S}'''_{gen},U}$ and $R_{\dot{S}'''_{gen},V}$ at the cold or hot

wall corresponds to the composition of the corresponding signs of $R_{T,U}$ and $R_{T,V}$ with the sign of $R_{\dot{S}'''_{gen},T}$ at the same wall.

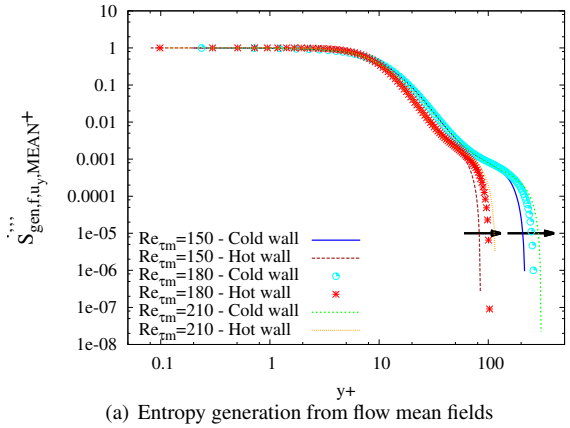

(a) Entropy generation from flow mean fields

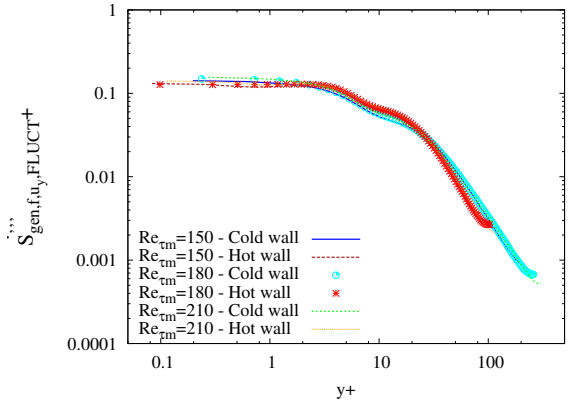

(b) Entropy generation from fluctuations

Figure 12: Decomposition of the dimensionless mean local entropy generation rate by vertical heat conduction (cf. Eqs. 25 and 26). The black arrows indicate the direction of change as $Re_{\tau m}$ increases.

The mean local entropy generation rate due to viscous friction $\left\langle \dot{S}'''_{gen,f} \right\rangle$ is increased whatever the distance to the walls when the mean friction Reynolds number is raised. The main contributor to $\dot{S}'''_{gen,f}$ near the walls and to the total entropy generation rate by viscous friction $\dot{S}_{gen,f}$ in the whole channel is due to the vertical gradient of the streamwise velocity and can be decomposed into its parts due to the mean fields (temperature, streamwise velocity, dynamic viscosity) $\dot{S}'''_{gen,f,u_y,MEAN}$ and to the fluctuations of these fields $\dot{S}'''_{gen,f,u_y,FLUCT}$. Both parts, in real value (dimensioned), also increase with the mean friction Reynolds number, whatever the ordinate. In dimensionless form (Figs.12), the fluctuating relative part (Fig. 12(b)) is almost unchanged when the mean friction Reynolds number is increased from 150 to 210. It is not the same for the dimensionless part due to mean fields (Fig. 12(a)) that increases with $Re_{\tau m}$ in the logarithmic and outer regions, in agreement with the corresponding increase in friction Reynolds numbers at the cold and hot walls (see Table B.1 in Appendix A). The position of the zero of $\dot{S}'''_{gen,f,u_y,MEAN}$ is unchanged in real values when $Re_{\tau m}$ is varied (it is located $\approx 0.03h$ from the center on the hot side of the channel) but its dimensionless distances to the walls are shifted further from the walls when increasing $Re_{\tau m}$ (y^+ is multiplied by 1.4 i.e., the $Re_{\tau m}$ ratio 210/140) as are the dimensionless positions of the mean maximum longitudinal velocity and the zero of its gradient.

3.3. *Influence of the thermal boundary condition type*

In this section, the wall-temperature ratio is set to $T_2/T_1 = 2$ and the mean friction Reynolds number to $Re_{\tau m} = 180$. Two Direct Numerical Simulations are carried out to analyze the influence of the thermal boundary condition type on the entropy generation rate statistics. In the first simulation, the "Fixed temperatures" case, the wall temperatures are set uniform and constant ($T_1 = 293\ K$ and $T_2 = 586\ K$). The resulting mean heat flux observed at the walls is then used as thermal boundary condition for a comparable simulation, named "Fixed heat flux", where the heat flux density is set to a uniform and constant value ($\approx 1700\ W.m^{-2}$).

The mean local entropy generation rate is slightly affected by the type of thermal boundary condition (Fig. 13(a)). Near the walls (Figs. 13(b) and 13(c)), $\left\langle \dot{S}'''_{gen} \right\rangle$ is a little smaller if wall heat flux density is fixed when compared to the fixed wall-temperature case (≈ -9 % at the walls). In the rest of the channel, both thermal boundary condition types result in very close mean entropy generation rates, although slightly larger when wall heat fluxes are fixed, in particular in the central region of the channel on the hot side ($\approx +3$ % at $y = h$ and $\approx +5$ % at $y = 3h/2$, h being the channel half-height).

Contrary to what is observed (by varying T_2/T_1 in Section 3.1 or $Re_{\tau m}$ in Section 3.2), the root-mean-square of the entropy generation rate behaves differently than its mean in the wall vicinities when heat flux density is fixed at the walls (Fig. 14). Near the cold wall, the standard deviation of the entropy generation rate exhibits a local maximum (around $y^+ \approx 5$) and then drops abruptly when getting closer to the wall (≈ -70 %) to reach ≈ 20 % of the entropy generation rate root-mean-square of the "Fixed temperatures" case at the cold wall. Near the hot wall, the local maximum is located at $y^+ \approx 6$, the relative drop is ≈ -90 % and the

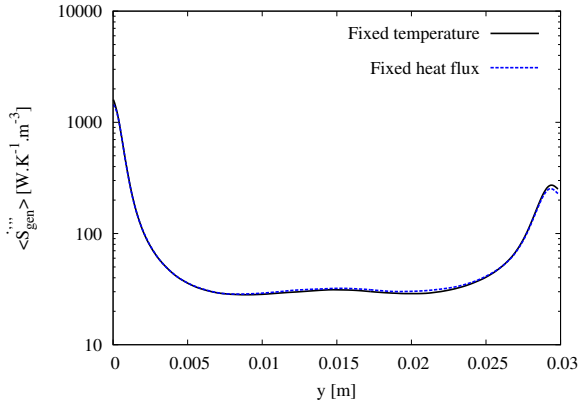

(a) $< \dot{S}'''_{gen} >$ for two thermal boundary condition types.

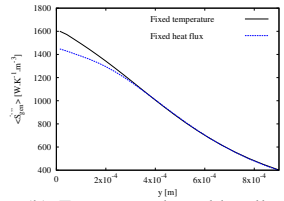

(b) Zoom near the cold wall.

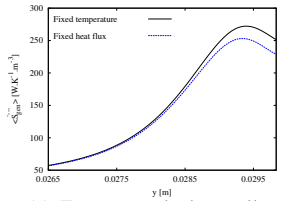

(c) Zoom near the hot wall.

Figure 13: Mean local entropy generation rate for two types of boundary conditions. $T_2/T_1 \approx 2$ and $Re_{\tau m} = 180$. Zooms near the cold wall (Left) and hot wall (right) are presented with linear ordinates for better readability.

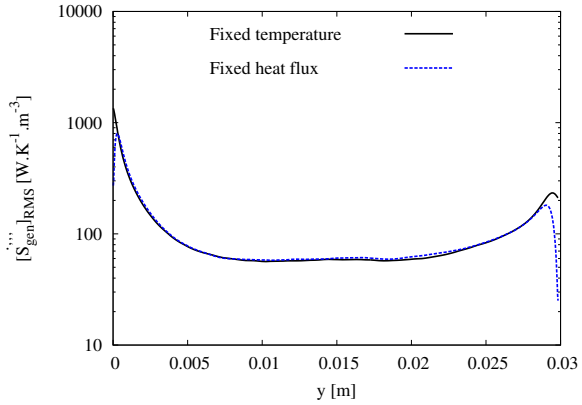

Figure 14: Root-mean-square of the local entropy generation rate for two types of boundary conditions ($T_2/T_1 \approx 2$ and $Re_{\tau m} = 180$).

root-mean-square at the wall $\approx$ 12 % of the magnitude observed when temperatures are fixed at the hot wall.

This sharp decrease of $\left[\dot{S}'''_{gen}\right]_{rms}$ near the walls in the fixed heat flux density case can be explained by the analysis of the entropy generation rate by vertical heat transfer (the majority term near the walls) once subdivided into its parts due to mean fields and to turbulent

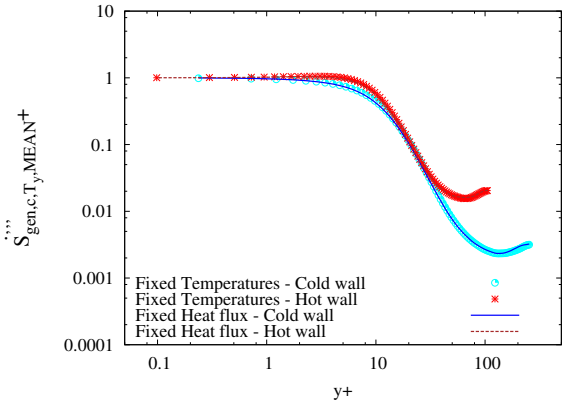

(a) Entropy generation from flow mean fields

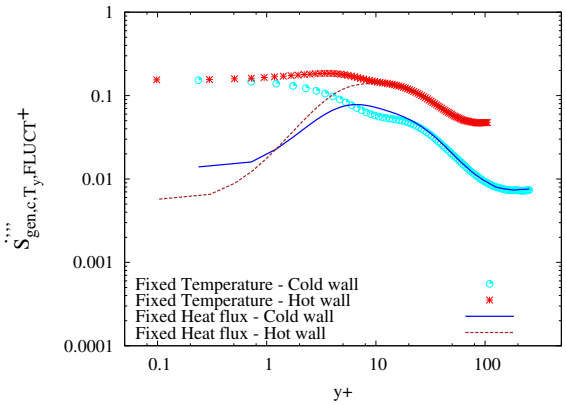

(b) Entropy generation from fluctuations

Figure 15: Decomposition of the dimensionless mean local entropy generation rate by vertical heat conduction (cf. Eqs. 22 and 23)

fluctuations (Figs. 15). The mean vertical heat transfer entropy generation rate due to mean thermal fields (the mean temperature, thermal conductivity and vertical component of the temperature gradient) is practically independent on the thermal boundary condition type (Fig. 15(a)). It is not the same for the relative part due to turbulent fluctuations of these fields (Fig. 15(b)) that is significantly smaller near the walls when heat flux density is fixed at the walls. This fluctuating part represents about 15 % of the mean field entropy generation rate (normalized to 1 after scaling) when the temperature is fixed at the walls. This relative value is only 1.4 % and 0.6 % at the cold and hot walls respectively when the wall heat flux density is imposed. The same qualitative drop of the fluctuating part in the mean entropy generation rate due to vertical heat transfer in the fixed wall heat flux case is observed for a different wall-temperature ratio $T_2/T_1 = 1.5$ (Fig. 16). Moreover, the relative proportion of the fluctuating part is even lower

than at $T_2/T_1 = 2$: 0.5 % and 0.3 % at the cold and hot walls respectively, while this proportion is always $\approx$ 15 % if temperatures are fixed at the walls.

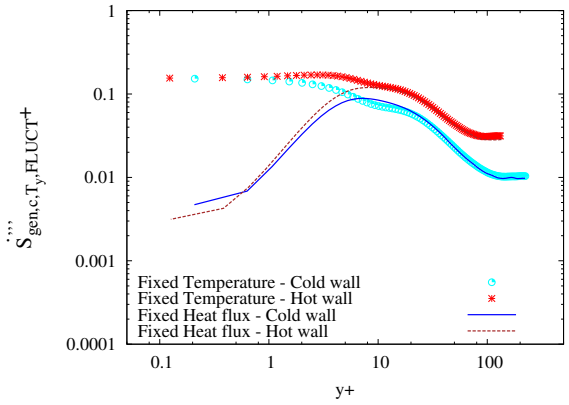

Figure 16: Dimensionless entropy generation from fluctuations in the mean entropy generation rate due to the vertical conduction of heat. Case where the parietal temperature ratio is 1.5.

This significant difference in the relative share due to near-wall fluctuations, depending on the type of thermal boundary condition, stems from the nature of the terms that fluctuate and those that remain constant over time. Indeed, when the temperatures are fixed at the walls, the entropy generation rate majority term $\left\langle \dot{S}'''_{gen,c,T_y} \right\rangle = \left\langle (k/T^2)(\partial T/\partial y)^2 \right\rangle$ includes at the walls a fixed term k/T^2 and a fluctuating term $(\partial T/\partial y)^2$. The relative standard deviation of this fluctuating factor is $\left[(\partial T/\partial y)^2\right]_{RMS} / \left\langle (\partial T/\partial y)^2 \right\rangle \approx 70$ % at the cold and hot walls when the wall-temperature ratio is $T_2/T_1 = 2$. If now heat flux is fixed at the walls, $\left\langle \dot{S}'''_{gen,c,T_y} \right\rangle = \left\langle q''^2/(kT^2) \right\rangle$ (where $q'' = -k\partial T/\partial y$ is the wall heat flux density) is composed of the fixed factor q''^2 and the fluctuating term $1/(kT^2)$. In this second case, the relative standard deviation of the fluctuating factor is only $\left[1/(kT^2)\right]_{RMS} / \left\langle 1/(kT^2) \right\rangle \approx 15$ % and 10 % at the cold and hot walls respectively, still in the $T_2/T_1 = 2$ case.

Contrary to the case where temperatures are imposed at the walls, the correlation coefficient between the local rate of entropy generation and the temperature $R_{\dot{S}'''_{gen},T}$ (Fig. 17(a)) is systematically negative near the walls when the wall heat flux density is imposed (≈ -0.8 at the walls). Indeed, a positive fluctuation with respect to the average very close to the wall ($T' > 0$) must be balanced by an increase of the local temperature at the wall ($T'_w > 0$) in such a way that the local heat flow (q''_w) remains constant there. This leads to a decrease in the local wall entropy generation rate induced by the decrease of its major component ($q''^2_w/(k_w T^2_w)$). The inversion of

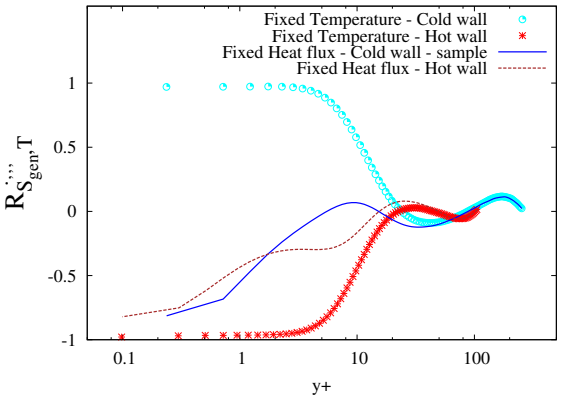

(a) Correlation with the temperature

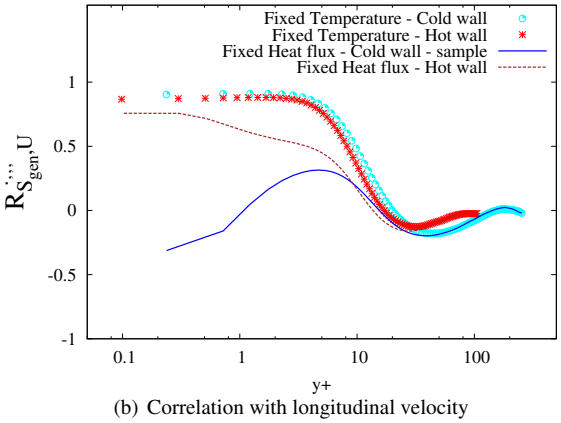

(b) Correlation with longitudinal velocity

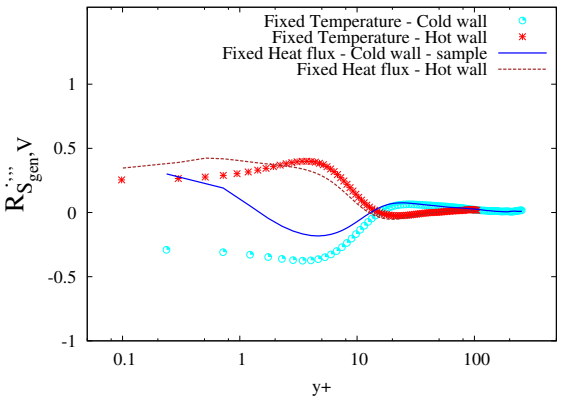

(c) Correlation with wall-normal velocity

Figure 17: Correlation coefficients of the local entropy generation rate with the temperature (a), the streamwise velocity component (b) and the wall-normal velocity component (c).

the sign of $R_{\dot{S}'''_{gen},T}$ near the cold wall when the thermal boundary condition changes from "fixed wall temperatures" to "imposed wall heat flux density" causes the same inversion for $R_{\dot{S}'''_{gen},U}$ and $R_{\dot{S}'''_{gen},V}$, always near the

cold wall. For example, at imposed parietal temperatures, the correlation between the local rate of entropy generation and the longitudinal component of velocity is always positive near the walls. At imposed heat flux density, this correlation remains positive near the hot wall but becomes negative near the cold wall. Similarly, whereas at imposed wall temperatures, the correlation of the local entropy generation rate with the wall-normal velocity component is negative near the cold wall and positive near the hot wall, the situation is reversed at the cold wall when heat flux density is fixed and the correlation coefficient $R_{\dot{S}'''_{gen},V}$ becomes positive at both walls.

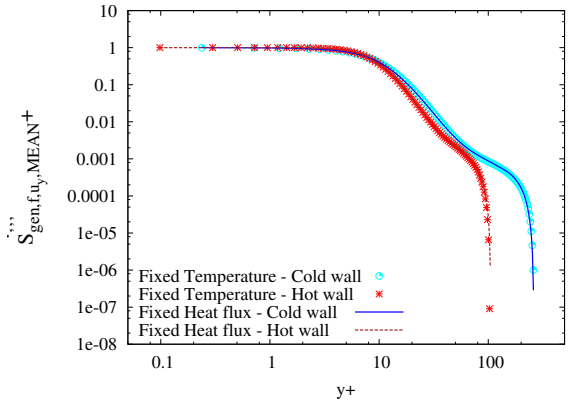

(a) Entropy generation from flow mean fields

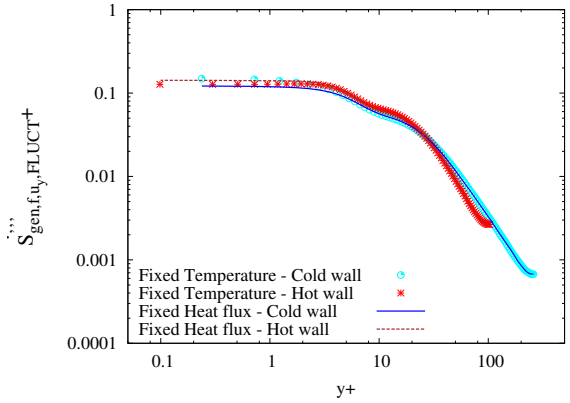

(b) Entropy generation from fluctuations

Figure 18: Decomposition of the dimensionless mean local entropy generation rate by vertical heat conduction (cf. Eqs. 25 and 26).

The dimensionless viscous friction entropy generation rate majority component profile ($\dot{S}'''_{gen,f,u_y}$) is not influenced significantly by the type of thermal boundary condition (Fig.18). The relative part related to the fluctuations of the velocity and temperature fields (Fig. 18(b)) is, however, a little lower at the cold wall and higher at the hot wall when the heat flux density is imposed on the walls.

3.4. *Influence of mean thermodynamic pressure*

In this section, the wall-temperature ratio is fixed at $T_2/T_1 = 2$, the temperatures being set to uniform and constant values $T_1 = 293\ K$ and $T_2 = 586\ K$ at the cold and hot wall respectively. The mean friction Reynolds number is set to $Re_{\tau m} = 180$. Three Direct Numerical Simulations are performed to analyze the influence of the mean thermodynamic pressure $\langle P_{th} \rangle$ on the entropy generation statistics: $\langle P_{th} \rangle = 1\ bar$, $1.5\ bar$ and $3\ bar$. This change is made into the initial conditions of the simulations (along with the initialization of the velocity and temperature profiles) by setting the initial thermodynamic pressure in the channel $P_{th,0}$. In the Low Mach approximation, the thermodynamic pressure is uniform in the channel (Eq. 4) but may change over time when temperatures are fixed at the walls. Indeed, the time derivative of the thermodynamic pressure is linked to the instantaneous net heat flux through the walls (Eq. 28, in a bi-periodic channel, where V_Ω is the domain volume). Nevertheless, the standard deviation of the thermodynamic pressure is relatively small (less than 0.4 % of the mean value) in the presented simulations. In addition, the mean dynamical pressure $\left\langle P_{dyn} \right\rangle$ in the momentum equation (Eq. 2) is very small when compared to the mean thermodynamic pressure (less than 0.2 %). For these reasons, the initial thermodynamic pressure $P_{th,0}$ is a very good indicator of the mean total pressure $\langle P \rangle = \left\langle P_{dyn} \right\rangle + \langle P_{th} \rangle$ in the channel, the relative gap being less than 1.7 %.

$$\frac{dP_{th}}{dt} = -\frac{\gamma - 1}{V_\Omega} \iint_{walls} q'' dA \tag{28}$$

When the initial thermodynamic pressure is varied from 1 *bar* to 3 *bar*, no significant change is observed on the profiles of the local entropy generation rate mean, root-mean-square and correlations with the temperature and the streamwise or wall-normal velocity components, and it is the same for the part of entropy generation due to heat conduction $\dot{S}'''_{gen,c}$ (Eq. 12). Conversely, the mean local entropy generation rate due to viscous friction $\dot{S}'''_{gen,f}$ (Eq. 11) decreases when the initial thermodynamic pressure is larger, whatever the distance to the walls (Fig. 19). Indeed, the change of the initial thermodynamic pressure is done at constant Reynolds number and wall temperatures. The mass flow rate crossing the channel is also unchanged, but the average density is increased when the mean pressure is larger for the same temperatures: this corresponds to lower bulk velocity (the bulk Reynolds number remains stable because the

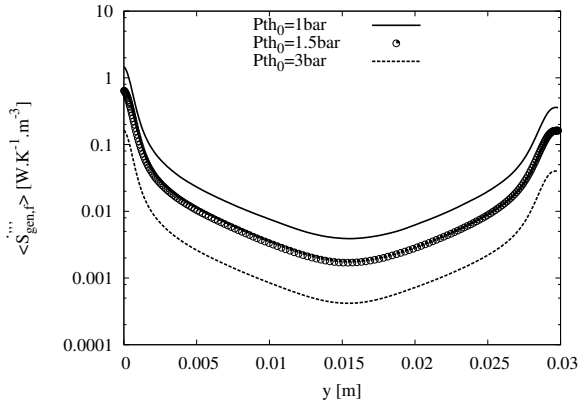

Figure 19: Mean local viscous friction entropy generation rate for three initial thermodynamic pressure ($P_{th,0}$ = 1 *bar*, 1.5 *bar* and 3 *bar*).

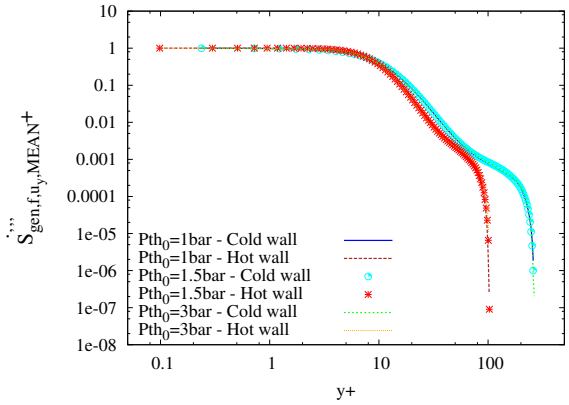

(a) Entropy generation from flow mean fields

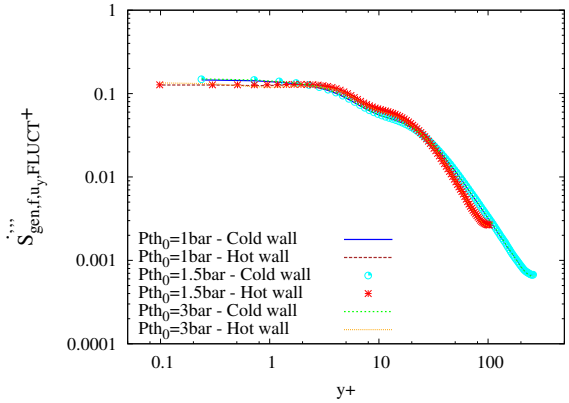

(b) Entropy generation from fluctuations

Figure 20: Decomposition of the dimensionless mean local entropy generation rate by viscous friction (cf. Eqs. 25 and 26)

kinematic viscosity is also decreasing), lower friction velocities and lower entropy generation rates due to viscous friction. When the mean pressure in the channel is raised from $\approx$ 1 *bar* to $\approx$ 3 *bar*, the hot and cold wall friction velocities are divided by 3 (see Table A.1). The entropy generation rates at the cold and hot walls are divided by ≈ 9 (the square of the multiplication factor applied to the pressure): the change in entropy generation due to viscous friction at the walls is primarily due to the variation of the vertical gradient of the mean streamwise velocity and its formula ($\dot{S}'''_{gen,f,u_y,MEAN}$ in Eq. 25) combined with the law at the wall $< U >^+ = y^+$ results in the square relationship just cited. Since the viscous friction relative part in entropy generation is very small, its decrease does not significantly alter the total entropy generation rate. Once made dimensionless, $\left\langle \dot{S}'''_{gen,f,u_y} \right\rangle$ and its components due to mean fields (Fig. 20(a)) and fluctuations (Fig. 20(b)) are almost unchanged by the variation of the mean thermodynamic pressure.

4. Conclusion

In this paper, Direct Numerical Simulations are performed for forced convective turbulent channel flows of a thermo-dependent gas subjected to high temperature gradients created by asymmetrical heating boundary conditions. The density, viscosity and thermal conductivity of the fluid depend on temperature. The thermal boundary conditions and key flow characteristics are varied separately with respect to a reference simulation in order to analyze the impact on the local entropy generation rate statistics. The hot to cold wall temperature ratio is varied from 1.5 to 3.0 (reference: 2.0), the mean friction Reynolds number from 150 to 210 (reference: 180), the mean thermodynamic pressure from 1 *bar* to 3 *bar* (reference 1.5 *bar*) and two thermal boundary condition types are applied (fixed wall temperatures, which corresponds to the reference simulation, on the one hand, and fixed wall heat flux density, on the other hand). The influence of these parameters on the local entropy generation rate statistics is studied (its mean, its root-mean-square and its correlations with the temperature and the streamwise or wall-normal velocity). In addition, the main components in the entropy generation rate are analyzed in more detail for their part due to mean fields (in particular the mean temperature), on the one hand, and their part due the fluctuations of these fields, on the other hand.

The parameters studied all affect the entropy generation rate statistics, but in a different way. An increase in the wall temperature ratio results in larger entropy generation rates throughout the flow channel, and to an increase in the asymmetry between the cold wall (where

the highest entropy generation rates are located) and the hot wall. At a fixed wall temperature ratio, increasing the mean friction Reynolds number leads to an increase in the entropy generation rate essentially near the walls, with little impact in the central area of the channel. If only the mean thermodynamic pressure is increased, the entropy generation rate due to viscous friction is decreased, with a negligible effect on the total entropy generation rate because of the overwhelming relative importance of the heat transfer entropy generation rate that is not impacted by the change in pressure. Changing the type of thermal boundary condition has a significant impact on the thermally induced fluctuations of the entropy generation rate near the walls (in the viscous and buffer sublayers), which are much less important at imposed wall temperatures than at fixed heat flux density. Similarly, the thermal boundary condition type influences the correlation coefficients of the entropy generation rate with the temperature or the streamwise or wall-normal velocity, while the wall temperature ratio or the mean friction Reynolds number have little influence on these coefficients. The sign of these correlations is inversed near the cold wall when switching from fixed wall temperatures to fixed wall heat flux. The presented Direct Numerical Simulations provide a detailed insight beyond the mere observation of the total entropy generation rate in the channel by establishing how the spatial distribution of the local entropy generation rate is modified by the parameters studied, in which direction and with which sensitivity.

5. Acknowledgment

This work was supported by French "Investments for the future" ("Investissements d'Avenir") programme managed by the National Agency for Research (ANR) under contract ANR-10-LABX-22-01 (labex SOLSTICE). This work was granted access to the HPC resources of CINES under the allocation 2020-A0062A05099 and 2021-A0082A05099 made by GENCI.

6. References

[1] Sarifuddin, S. Chakravarty, P. K. Mandal, Effect of heat and mass transfer on non-Newtonian flow - Links to atherosclerosis, International Journal of Heat and Mass Transfer 52 (2009) 5719–5730. doi:10.1016/j.ijheatmasstransfer.2009.04.040.

[2] N. Mao, S. Mengjie, P. Dongmei, D. Shiming, Computational fluid dynamics analysis of convective heat transfer coefficients for a sleeping human body, Applied Thermal Engineering 117 (2017) 385–396. doi:10.1016/j.applthermaleng.2017.02.012.

[3] C. Zhao, B. E. Hobbs, A. Ord, Advances in convective and advective heat transfer in geological systems, Journal of Geochemical Exploration 101(1) (2009) 128. doi:10.1016/j.gexplo.2008.11.002.

[4] A. Costa, O. Melnik, E. Vedeneeva, Thermal effects during magma ascent in conduits, Journal of Geophysical Research 112 (2007) B12205. doi:10.1029/2007JB004985.

[5] A. Mitsuishi, M. Sakoh, T. Shimura, K. Iwamoto, A. Murata, H. Mamori, Direct numerical simulation of convective heat transfer in a pipe with transverse vibration, International Journal of Heat and Mass Transfer 148 (2019) 119048. doi:10.1016/j.ijheatmasstransfer.2019.119048.

[6] S. Javed, H. M. Ali, H. Babar, S. Khan, M. M. Janjua, M. A. Bashir, Internal convective heat transfer of nanofluids in different flow regimes: A comprehensive review, Physica A: Statistical Mechanics and its Applications 538 (2020) 122783. doi:10.1016/j.physa.2019.122783.

[7] T. Defraye, B. Blocken, J. Carmeliet, CFD analysis of convective heat transfer at the surfaces of a cube immersed in a turbulent boundary layer, International Journal of Heat and Mass Transfer 53 (2010) 297–308. doi:10.1016/j.ijheatmasstransfer.2009.09.029.

[8] Y. Liu, H. Wu, An experimental investigation on the unsteady heat transfer process over an ice accreting airfoil surface, International Journal of Heat and Mass Transfer 122 (2018) 707–718. doi:10.1016/j.ijheatmasstransfer.2018.02.023.

[9] D. V. Guzei, A. V. Minakov, V. Y. Rudyak, On efficiency of convective heat transfer of nanofluids in laminar flow regime, International Journal of Heat and Mass Transfer 139 (2019) 180–192. doi:10.1016/j.ijheatmasstransfer.2019.05.016.

[10] S. K. Kim, Forced convection heat transfer for the fully-developed laminar flow of the cross fluid between parallel plates, Journal of Non-Newtonian Fluid Mechanics 276 (2020) 104226. doi:10.1016/j.jnnfm.2019.104226.

[11] A. I. Bashir, M. Everts, R. Bennacer, J. P. Meyer, Single-phase forced convection heat transfer and pressure drop in circular tubes in the laminar and transitional flow regimes, Experimental Thermal and Fluid Science 109 (2019) 109891. doi:10.1016/j.expthermflusci.2019.109891.

[12] C. Wang, P. Gao, S. Tan, Z. P. Wang, Forced convection heat transfer and flow characteristics in laminar to turbulent transition region in rectangular channel, Experimental Thermal and Fluid Science 44 (2013) 490–497. doi:10.1016/j.expthermflusci.2012.08.010.

[13] Z. Parlak, N. Parlak, Y. slamolu, Optimal design of a converging diverging channel for convective heat transfer enhancement in fully developed turbulent air flow, International Journal of Thermal Sciences In Press, Corrected Proof (2020) 106732. doi:10.1016/j.ijthermalsci.2020.106732.

[14] R. K. Ajeel, W.-I. Salim, K. Hasnan, Experimental and numerical investigations of convection heat transfer in corrugated channels using alumina nanofluid under a turbulent flow regime, Chemical Engineering Research and Design 148 (2019) 202–217. doi:10.1016/j.cherd.2019.06.003.

[15] I. V. Miroshnichenko, M. A. Sheremet, Turbulent natural convection heat transfer in rectangular enclosures using experimental and numerical approaches: A review, Renewable and Sustainable Energy Reviews 82 (2018) 40–59. doi:10.1016/j.rser.2017.09.005.

[16] J. Haervig, H. Sorensen, Natural convective flow and heat transfer on unconfined isothermal zigzag-shaped ribbed vertical surfaces, International Communications in Heat and Mass Transfer 119 (2020) 104982. doi:10.1016/j.icheatmasstransfer.2020.104982.

[17] R. C. Adhikari, D. H. Wood, M. Pahlevani, An experimental and

numerical study of forced convection heat transfer from rectangular fins at low reynolds numbers, International Journal of Heat and Mass Transfer 163 (2020) 120418. doi:10.1016/j.ijheatmasstransfer.2020.120418.

[18] H. J. Kim, H. S. Yoon, Forced convection heat transfer from the biomimetic cylinder inspired by a harbor seal vibrissa, International Journal of Heat and Mass Transfer 117 (2018) 548–558. doi:10.1016/j.ijheatmasstransfer.2017.10.053.

[19] M.-S. Chae, B.-J. Chung, Variations in buoyancy-aided turbulent mixed convective heat transfer along a vertical rectangular channel, International Communications in Heat and Mass Transfer 118 (2020) 104906. doi:10.1016/j.icheatmasstransfer.2020.104906.

[20] D. Liu, H. Gu, Mixed convection heat transfer in a 5×5 rod bundles, International Journal of Heat and Mass Transfer 113 (2017) 914–921. doi:10.1016/j.ijheatmasstransfer.2017.05.113.

[21] A. M. Hussein, H. K. Dawood, R. A. Bakara, K. Kadirgamaa, Numerical study on turbulent forced convective heat transfer using nanofluids TiO_2 in an automotive cooling system, Case Studies in Thermal Engineering 9 (2017) 72–78. doi:10.1016/j.csite.2016.11.005.

[22] H. Pu, S. Li, S. Jiao, M. Dong, Y. Shang, Numerical investigation on convective heat transfer to aviation kerosene flowing in vertical tubes at supercritical pressures, International Journal of Heat and Mass Transfer 118 (2018) 857–871. doi:10.1016/j.ijheatmasstransfer.2017.11.029.

[23] Q. Dai, X. Fang, Y. Xu, Numerical study of forced convective heat transfer around a spherical aerostat, Advances in Space Research 52(12) (2013) 2199–2203. doi:10.1016/j.asr.2013.09.004.

[24] K. Hadad, A. Rahimian, M. R. Nematollahi, Numerical study of single and two-phase models of water/Al_2O_3 nanofluid turbulent forced convection flow in VVER-1000 nuclear reactor, Annals of Nuclear Energy 60 (2013) 287–294. doi:10.1016/j.anucene.2013.05.017.

[25] D. Angeli, I. Di Piazza, R. Marinari, E. Stalio, Fully developed turbulent convection of lead bismuth eutectic in the elementary cell of the NACIE-UP fuel pin bundle, Nuclear Engineering and Design 356 (2020) 110366. doi:10.1016/j.nucengdes.2019.110366.

[26] Y.-T. Wu, C. Chen, B. Liu, C.-F. Ma, Investigation on forced convective heat transfer of molten salts in circular tubes, International Communications in Heat and Mass Transfer 39 (2012) 1550–1555. doi:10.1016/j.icheatmasstransfer.2012.09.002.

[27] S. Siegrist, H. Stadler, B. Hoffschmidt, Wind tunnel measurements of forced convective heat loss from multi-megawatt cavities of solar central receiver systems, Solar Energy 169 (2018) 607–615. doi:10.1016/j.solener.2018.04.029.

[28] W. H. Azmi, K. V. Sharma, P. K. Sarma, R. Mamat, S. Anuar, V. D. Rao, Experimental determination of turbulent forced convection heat transfer and friction factor with SiO_2 nanofluid, Experimental Thermal and Fluid Science 51 (2013) 103–111. doi:10.1016/j.expthermflusci.2013.07.006.

[29] D. P. Soman, S. Karthika, P. Kalaichelvi, T. K. Radhakrishnan, Experimental study of turbulent forced convection heat transfer and friction factor in dimpled plate heat exchanger, Applied Thermal Engineering 162 (2019) 114254. doi:10.1016/j.applthermaleng.2019.114254.

[30] A. V. Minakov, D. V. Guzei, K. N. Meshkov, I. A. Popov, A. V. Shchelchkov, Experimental study of turbulent forced convection of nanofluid in channels with cylindrical and spherical hollows, International Journal of Heat and Mass Transfer 115 (2017) 915–025. doi:10.1016/j.ijheatmasstransfer.2017.07.117.

[31] M. Basha, N. A. C. Sidik, Numerical predictions of laminar and turbulent forced convection: Lattice Boltzmann simulations using parallel libraries, International Journal of Heat and Mass Transfer 116 (2018) 715–724. doi:10.1016/j.ijheatmasstransfer.2017.09.072.

[32] D. Huu-Quan, A. M. Rostami, M. S. Rad, M. Izadi, A. Hajjar, Q. Xiong, 3D numerical investigation of turbulent forced convection in a double-pipe heat exchanger with flat inner pipe, Applied Thermal Engineering 182 (2020) 116106. doi:10.1016/j.applthermaleng.2020.116106.

[33] J. E. Jaramillo, C. D. Prez-Segarra, A. OLiva, K. Claramunt, Analysis of different RANS models applied to turbulent forced convection, International Journal of Heat and Mass Transfer 50 (2007) 3749–3766. doi:10.1016/j.ijheatmasstransfer.2007.02.015.

[34] A. M. Oler, C. E. Clifford, M. L. Kimber, Quantitative assessment of eddy viscosity RANS models for turbulent mixed convection in a differentially heated plane channel, International Journal of Heat and Mass Transfer 161 (2020) 120313. doi:10.1016/j.ijheatmasstransfer.2020.120313.

[35] S. Kumar, B. Premachandran, P. M. V. Subbarao, Large eddy simulation of single-phase forced convection in pillow plate channel with periodic boundary conditions, International Journal of Heat and Mass Transfer 149 (2020) 119176. doi:10.1016/j.ijheatmasstransfer.2019.119176.

[36] I. K. Kim, H. S. Yoon, Large eddy simulation of forced convection heat transfer from wavy cylinders with different wavelengths, International Journal of Heat and Mass Transfer 127(C) (2018) 683–700. doi:10.1016/j.ijheatmasstransfer.2018.08.092.

[37] S. Serra, A. Toutant, F. Bataille, Thermal Large Eddy Simulation in a very simplified geometry of a solar receiver, Heat Transfer Engineering 33(6) (2012) 505–524. doi:10.1080/01457632.2012.624856.

[38] R. W. Hill, K. S. Ball, Direct numerical simulations of turbulent forced convection between counter-rotating disks, International Journal of Heat and Fluid Flow 20(3) (1999) 208–221. doi:10.1016/S0142-727X(99)00010-7.

[39] J. Liu, P. Zhao, M. Lei, S. Yang, H. Nemati, Numerical investigation of spatial-developing turbulent heat transfer in forced convections at different supercritical pressures, International Journal of Heat and Mass Transfer 159 (2020) 120128. doi:10.1016/j.ijheatmasstransfer.2020.120128.

[40] S. A. Orzag, Analytical theories of turbulence, Journal of Fluid Mechanics 41(02) (1970) 363–386. doi:10.1017/S0022112070000642.

[41] J. Kim, P. Moin, R. Moser, Turbulence statistics in fully developed channel flow at low Reynolds number, Journal of Fluid Mechanics 177 (1987) 133–166. doi:10.1017/S0022112087000892.

[42] B. Zhou, M. Yang, Z. Li, Z. Wang, Y. Zhang, Numerical simulations of forced convection across a single tube to evaluate applicability of the DNS, LES and RSM methods, Applied Thermal Engineering 123 (2017) 123–130. doi:10.1016/j.applthermaleng.2017.05.055.

[43] P. Moin, K. Mahesh, DIRECT NUMERICAL SIMULATION: A tool in turbulence researchs, Annual Review of Fluid Mechanics 30 (1998) 539–578. doi:10.1146/annurev.fluid.30.1.539.

[44] B. Karnk, N. Fehn, W. A. Wall, M. Kronbichler, A high-order semi-explicit discontinuous Galerkin solver for 3D incompressible flow with application to DNS and LES of turbulent channel flow, Journal of Computational Physics 348 (2017) 634–659. doi:10.1016/j.jcp.2017.07.039.

[45] M. Piller, Direct numerical simulation of turbulent forced convection in a pipe, Internatinal Journal for Numerical Methods in Fluids 49 (2005) 583–602. doi:10.1002/fld.994.

[46] D. Modesti, S. Pirozzoli, F. Grasso, Direct numerical simulation of developed compressible flow in square ducts, International Journal of Heat and Fluid Flow 76 (2019) 130–140. doi:10.1016/j.ijheatfluidflow.2019.02.002.

[47] P. G. Huang, G. N. Coleman, P. Bradshaw, Compressible turbulent channel flows: DNS results and modeling, Journal of Fluid Mechanics 305 (1995) 185–218. doi:10.1017/S0022112095004599.

[48] Y. Morinishi, S. Tamano, E. Nakamura, New scaling of turbulence statistics for incompressible thermal channel flow with different total heat flux gradients, International Journal of Heat and Mass Transfer 50 (9-10) (2007) 1781–1789. doi:10.1016/j.ijheatmasstransfer.2006.10.012.

[49] H. Kawamura, H. Abe, Y. Matsuo, DNS of turbulent heat transfer in channel flow with respect to Reynolds and Prandtl number effects, International Journal of Heat and Fluid Flow 20 (1999) 196–207. doi:10.1016/s0142-727x(99)00014-4.

[50] C. Flageul, S. Benhamadouche, E. Lamballais, D. Laurence, DNS of turbulent channel flow with conjugate heat transfer: Effect of thermal boundary conditions on the second moments and budgets, International Journal of Heat and Fluid Flow 55 (2015) 34–44. doi:10.1016/j.ijheatfluidflow.2015.07.009.

[51] L. Redjem-Saad, M. Ould-Rouiss, G. Lauriat, Direct numerical simulation of turbulent heat transfer in pipe flows: Effect of Prandtl number, International Journal of Heat and Fluid Flow 28 (2007) 847–861. doi:10.1016/j.ijheatfluidflow.2007.02.003.

[52] F. Aulery, A. Toutant, F. Bataille, Y. Zhou, Energy transfer process of anisothermal wall-bounded flows, Physics Letters A 379(24-25) (2015) 1520–1526. doi:10.1016/j.physleta.2015.03.022.

[53] F. Aulery, D. Dupuy, A. Toutant, F. Bataille, Y. Zhou, Spectral analysis of turbulence in anisothermal channel flows, Computers & Fluids 151 (2017) 115–131. doi:10.1016/j.compfluid.2016.06.011.

[54] A. Toutant, F. Bataille, Turbulence statistics in a fully developed channel flow submitted to a high temperature gradient, International Journal of Thermal Sciences 74 (2013) 104–118. doi:10.1016/j.ijthermalsci.2013.06.003.

[55] X. Daguenet-Frick, J. M. Foucaut, S. Couderc, A. Toutant, G. Olalde, Experimental analysis of the turbulent flow behavior of a textured surface proposed for asymmetric heat exchangers, Flow Turbulence and Combustion 89(1) (2012) 149–169. doi:10.1007/s10494-012-9387-y.

[56] M. Bellec, A. Toutant, G. Olalde, Large eddy simulations of thermal boundary layer developments in a turbulent channel flow under asymmetrical heating, Computers and fluids 151 (2017) 159–176. doi:10.1016/j.compfluid.2016.07.001.

[57] S. Serra, A. Toutant, F. Bataille, Y. Zhou, Turbulent kinetic energy spectrum in very anisothermal flows, Physics Letters A 376(45) (2012) 3177–3184. doi:10.1016/j.physleta.2012.08.005.

[58] D. Dupuy, A. Toutant, F. Bataille, Turbulence kinetic energy exchanges in flows with highly variable fluid properties, Journal of Fluid Mechanics 834 (2018) 5–54. doi:10.1017/jfm.2017.729.

[59] D. Dupuy, A. Toutant, F. Bataille, Equations of energy exchanges in variable density turbulent flows, Physics Letters A 382(5) (2018) 327–333. doi:10.1016/j.physleta.2017.11.026.

[60] J. M. Avellaneda, F. Bataille, A. Toutant, DNS of turbulent low Mach channel flow under asymmetric high temperature gradient: Effect of thermal boundary condition on turbulence statistics, International Journal of Heat and Fluid Flow 77 (2019) 40–47. doi:10.1016/j.ijheatfluidflow.2019.03.002.

[61] A. Bejan, Entropy generation minimization, CRC Press, 1996, ISBN: 0-8493-9651-4.

[62] A. Bejan, A study of entropy generation in fundamental convective heat transfer, Transactions of the ASME 101 (1979) 505–524.

[63] A. Bejan, Entropy generation minimization: the new thermodynamics of finite-sized devices and finite-time processes, Journal of Applied Physics 79(3) (1996) 1191–1218. doi:10.1063/1.362674.

[64] T. A. Jankowski, Minimizing entropy generation in internal flows by adjusting the shape of the cross-section, International Journal of Heat and Mass Transfer 52 (2009) 3439–3445. doi:10.1016/j.ijheatmasstransfer.2009.03.016.

[65] H. Xiao, J. Wang, Z. Liu, W. Liu, Turbulent heat transfer optimization for solar air heater with variation method based on exergy destruction minimization principle, International Journal of Heat and Mass Transfer 136 (2019) 1096–1105. doi:10.1016/j.ijheatmasstransfer.2019.03.071.

[66] J.-M. Avellaneda, F. Bataille, A. Toutant, G. Flamant, Variational entropy generation minimization of a channel flow: Convective heat transfer in a gas flow, International Journal of Heat and Mass Transfer 160 (2020) 120168. doi:10.1016/j.ijheatmasstransfer.2020.120168.

[67] S. Jia, X. Cao, X. Yuan, K.-T. Yu, Multi-objective topology optimization for the solar thermal decomposition of methane reactor enhancement, Chemical Engineering Science In Press, Corrected Proof (2020) 116265. doi:10.1016/j.ces.2020.116265.

[68] J. Guo, L. Cheng, M. Xu, Optimization design of shell-and-tube heat exchanger by entropy generation minimization and genetic algorithm, Applied Thermal Engineering 29(14-15) (2009) 2954–2960. doi:10.1016/j.applthermaleng.2009.03.011.

[69] A. Ebrahimi-Moghadam, A. J. Moghadam, Optimal design of geometrical parameters and flow characteristics for Al_2O_3/water nanofluid inside corrugated heat exchangers by using entropy generation minimization and genetic algorithm methods, Applied Thermal Engineering 149 (2019) 889–898. doi:10.1016/j.applthermaleng.2018.12.068.

[70] A. Ebrahimi-Moghadam, B. Mohseni-Gharyehsafa, M. Farzaneh-Gord, Using artificial neural network and quadratic algorithm for minimizing entropy generation of Al_2O_3-EG/W nanofluid flow inside parabolic trough solar collector, Renewable Energy 129(A) (2018) 473–485. doi:10.1016/j.renene.2018.06.023.

[71] K. Alabi, F. Ladeinde, M. vonSpakovsky, D. Moorhouse, J. Camberos, Assessing CFD modeling of entropy generation for the air frame subsystem in an integrated aircraft design/synthesis procedure, in: 44th AIAA Aerospace Sciences Meeting and Exhibit, Reno, Nevada, 9-12 January, 2006. doi:10.2514/6.2006-587.

[72] F. Kock, H. Herwig, Entropy production calculation for turbulent shear flows and their implementation in CFD codes, International Journal of Heat and Fluid Flow 26 (2005) 672–680. doi:10.1016/j.ijheatfluidflow.2005.03.005.

[73] S. Paolucci, On the filtering of sound from the Navier-Stokes equations, Tech. Rep. SAND82-8257, Livermore: Scandia National Laboratories.

[74] W. Sutherland, The viscosity of gases and molecular force, Philosophical Magazine Series 5 36:223 (1893) 507–531. doi:10.1080/14786449308620508.

[75] A. W. Vreman, J. G. M. Kuerten, Comparison of direct numerical simulation databases of turbulent channel flow at re_τ = 180, Physics of Fluids 26 (2014) 015102. doi:10.1063/1.4861064.

[76] R. D. Moser, Direct numerical simulation of turbulent channel flow up to $re_{\tau m}$ = 590, Physics of fluids 11 (1999) 943. doi:10.1063/1.869966.

[77] C. Calvin, O. Cueto, P. Emonot, An object-oriented approach to the design of fluid mechanics software, ESAIM: Mathematical Modeling and Numerical Analysis 36(05) (2002) 907–921. doi:10.1051/m2an:2002038.

[78] G. Bois, Direct numerical simulation of a turbulent bubbly flow in a vertical channel: Towards an improved second-order Reynolds stress model, Nuclear Engineering and Design 321 (2017) 92–103. doi:10.1016/j.nucengdes.2017.01.023.

[79] A. Toutant, E. Labourasse, O. Lebaigue, O. Simonin, DNS of the interaction between a deformable buoyant bubble and a spatially decaying turbulence: A priori tests for LES two-phase flow modelling, Computers & Fluids 37(7) (2008) 877–886. doi:10.1016/j.compfluid.2007.03.019.

[80] F. Kock, H. Herwig, Local entropy production in turbulent shear flows: a high-Reynolds number model with wall functions, International Journal of Heat and Mass Transfer 47 (2004) 2205–2215. doi:10.1016/j.ijheatmasstransfer.2003.11.025.

[81] J. M. Avellaneda, A. Toutant, G. Flamant, P. Neveu, F. Bataille, Entropy generation in nonisothermal flows: Influence of boundary condition type and intensity, Journal of Thermophysics and Heat Transferdoi:10.2514/1.T5748.

Nomenclature

$\dot{S}'''_{gen,f,u_y,FLUCT}$	Part of $\left\langle \dot{S}'''_{gen,f,u_y} \right\rangle$ due to fluctuations in Eqs. 25	$[W.K^{-1}.m^{-3}]$
$\dot{S}'''_{gen,c,T_y,FLUCT}$	Part of $\left\langle \dot{S}'''_{gen,c,T_y} \right\rangle$ due to fluctuations in Eqs. 22	$[W.K^{-1}.m^{-3}]$
$\dot{S}'''_{gen,c,T_y,MEAN}$	Part of $\left\langle \dot{S}'''_{gen,c,T_y} \right\rangle$ due to mean fields in Eqs. 22	$[W.K^{-1}.m^{-3}]$
$\dot{S}'''_{gen,c,T_y}$	Local entropy generation rate due to wall-normal heat conduction, Eqs. 13	$[W.K^{-1}.m^{-3}]$
$\dot{S}'''_{gen,c}$	Local entropy generation rate due to heat conduction in Eqs. 11 and 12	$[W.K^{-1}.m^{-3}]$
$\dot{S}'''_{gen,f,u_y,MEAN}$	Part of $\left\langle \dot{S}'''_{gen,f,u_y} \right\rangle$ due to mean fields in Eqs. 25	$[W.K^{-1}.m^{-3}]$
$\dot{S}'''_{gen,f,u_y}$	Local entropy generation rate due to viscous friction from the wall-normal gradient of the longitudinal velocity in Eq. 24	$[W.K^{-1}.m^{-3}]$
$\dot{S}'''_{gen,f}$	Local entropy generation rate due to viscous friction in Eqs. 11	$[W.K^{-1}.m^{-3}]$
$\dot{S}'''_{gen}$	Local entropy generation rate in Eq. 8	$[W.K^{-1}.m^{-3}]$
$\dot{S}_{gen,c}$	Total entropy generation rate due to heat conduction	$[W.K^{-1}]$
$\dot{S}_{gen,f}$	Total entropy generation rate due to viscous friction	$[W.K^{-1}]$
$\dot{S}_{gen}$	Total entropy generation rate , Eq. 10	$[W.K^{-1}]$
C_p	Thermal capacity	$[J.kg^{-1}.K^{-1}]$
h	Channel half-height	$[m]$
k	Thermal conductivity	$[W.m^{-1}.K^{-1}]$
Ma	Mach number	
P	Pressure , $P = P_{dyn} + P_{th}$	$[Pa]$
P_{dyn}	Dynamic pressure in Eq. 2	$[Pa]$
$P_{th,0}$	Initial thermodynamic pressure	$[Pa]$
P_{th}	Thermodynamic pressure , Eqs. 3 and 4	$[Pa]$
Pr	Prandtl number	
q''_w	Heat flux density at the walls	$[W.m^{-2}]$
r	Specific gas constant	$[J.kg^{-1}.K^{-1}]$
$R_{X,Y}$	Linear correlation coefficient between X and Y fluctuating quantities, see Eqs. 21	
$Re_{\tau m}$	Mean friction Reynolds number in Eqs. 15	
Re_τ	Friction Reynolds number in Eqs. 16	
t	time	$[s]$
T_τ	Friction temperature in Eqs. 18	$[K]$
U, V, W	Longitudinal, wall-normal an transversal components of the velocity	$[m.s^{-1}]$
U_i	Ith component of the instantaneous velocity vector in Eqs. 1 to 4	$[m.s^{-1}]$
$U_{\tau m}$	Mean friction velocity with $U_{\tau m} = (U_{\tau,cold} + U_{\tau,hot})/2$	$[m.s^{-1}]$
U_τ	Friction velocity in Eqs. 17	$[m.s^{-1}]$
x, y, z	Longitudinal, wall-normal and transversal Cartesian coordinates respectively	$[m]$
x_i	Ith Cartesian coordinate in Eqs. 1 to 4	$[m]$
y^+	Dimensionless distance from the closest wall in wall units (Eq. 27)	
T	Temperature	$[K]$

Δt^+	Dimensionless averaging time
Δt^+_{EGR}	Dimensionless averaging time for statistical quantities related to the entropy generation rate
$\Delta x^+, \Delta y^+, \Delta z^+$	Dimensionless mesh sizes in wall units in the longitudinal, wall-normal and transversal directions
γ	Heat capacity ratio
μ	Dynamic viscosity $[Pa.s]$
ϕ	Viscous dissipation function in Eq. 9 $[W.m^{-3}]$
ρ	Density $[kg.m^{-3}]$
$(\_)^+$	Dimensionless quantity as in Eqs.23 and 26
$(\_)'''$	Related to a quantity per unit of volume $[m^{-3}]$
$(\dot{\_})$	Related to a quantity derived with respect to time $[s^{-1}]$
T'	Local instantaneous fluctuation of temperature $T' = T - \langle T \rangle$ $[K]$
$(\_)_\tau$	Friction quantity
$(\_)_{cold}$	Subscript related to the channel cold plate
$(\_)_{FLUCT}$	Part of a quantity coming from the variances and correlations of its component turbulent fluctuations
$(\_)_{hot}$	Subscript related to the channel hot plate
$(\_)_{MEAN}$	Part of a quantity coming from mean fields of its components
$(\_)_m$	Subscript related to the a mean value between the cold and hot walls, as in $Re_{\tau m}$
$(\_)_{RMS}$	Root-mean-square of a fluctuating quantity as in Eq. 20
$(\_)_w$	Subscript related to a value at a wall
$< \_ >$	Statistical average over (xz) planes and over time as in Eq. 19

Appendix A. Friction characteristics

In this appendix, the friction velocities (Eq. 17), temperatures (Eq. 18) and Reynolds numbers (Eq. 16) are provided at the hot and the cold wall (see Table A.1). The names of the simulations are coded as follows: $Field1 Field2 - Field3(-Field4)$, where the four fields are defined hereunder. As an example, F180-2.0 corresponds to a fixed wall heat flux density simulation at mean friction Reynolds number 180 with a hot to cold wall temperature ratio of 2 and an initial uniform thermodynamic pressure of 1.5 bar. DNS name coding is as follows:

1. Field1: thermal wall boundary condition type: F=Fixed heat flux density, T=Fixed temperatures.
2. Field2: mean friction Reynolds number $Re_{\tau m}$.
3. Field3: hot to cold wall temperature ratio T_2/T_1.
4. Field4: an optional field: when present, it indicates the initial thermodynamic pressure. When missing, this pressure is $P_{th,0} = 1.5\ bar$.

Appendix B. Dimensionless mesh and time characteristics

In this appendix, the dimensionless mesh sizes and integration times (see Table B.1) are provided for each simulation, which names follow the same coding (see Appendix A). Δx and Δz are the longitudinal and transversal (uniform) mesh sizes respectively. Δy_{cold}, Δy_{hot} and Δy_{center} are the wall-normal mesh sizes at the cold and hot wall, and at the center of the channel respectively. These mesh sizes are normalized into wall unit magnitudes by ν/U_τ: the kinematic viscosity and the friction velocity are taken at the corresponding walls for Δy_{cold} and Δy_{hot}. The average $\nu_m = (\nu_{cold} + \nu_{hot})/2$ and $U_{\tau,m} = (U_{\tau,cold} + U_{\tau,hot})/2$ are used for the normalization of Δx, Δz and Δy_{center}. The integration times for the velocity and temperature statistics (Δt^+) and for the entropy generation rate statistics (Δt^+_{EGR}) are normalized by $h/U_{\tau,m}$, where h is the half-height of the channel.

Table A.1: DNS characteristics : friction quantities at the cold and hot walls.

	$U_{\tau,cold}\ [m.s^{-1}]$	$T_{\tau,cold}\ [K]$	$Re_{\tau,cold}$	$U_{\tau,hot}\ [m.s^{-1}]$	$T_{\tau,hot}\ [K]$	$Re_{\tau,hot}$
T180-1.5	0.154	3.0	226	0.183	3.7	133
T180-2.0	0.174	5.4	256	0.234	8.1	106
T180-2.5	0.186	7.5	275	0.275	12.8	87
T180-3.0	0.194	9.4	286	0.304	18.0	71
T150-2.0	0.144	5.6	213	0.194	8.3	87
T210-2.0	0.201	5.3	296	0.268	7.9	122
F180-2.0	0.174	5.4	257	0.235	8.0	108
F180-1.5	0.154	3.0	224	0.184	3.7	136
T180-2.0-1bar	0.262	5.4	257	0.351	8.2	106
T180-2.0-3bar	0.087	5.4	257	0.118	8.1	107

Table B.1: DNS characteristics: mesh definitions and averaging times in wall units.

	Δ_x^+	$\Delta_{y,cold}^+$	$\Delta_{y,center}^+$	$\Delta_{y,hot}^+$	Δ_z^+	Δt^+	Δt_{EGR}^+
T180-1.5	5.37	0.42	3.41	0.25	5.37	130	123
T180-2.0	4.63	0.47	2.94	0.20	4.63	431	113
T180-2.5	3.92	0.51	2.49	0.16	3.92	73	72
T180-3.0	3.30	0.53	2.10	0.13	3.30	53	52
T150-2.0	5.82	0.39	2.43	0.16	3.82	115	94
T210-2.0	5.32	0.55	3.39	0.22	5.32	141	117
F180-2.0	4.68	0.48	2.98	0.20	4.68	411	128
F180-1.5	5.44	0.42	3.46	0.25	5.44	90	90
T180-2.0-1bar	4.62	0.48	2.94	0.20	4.62	26	26
T180-2.0-3bar	4.65	0.48	2.96	0.20	4.65	51	51